

# Accelerator Physics\*

O. Boine-Frankenheim  
TEMF, TU Darmstadt

16.6.2013

## Contents

<b>1</b>	<b>Prerequisites</b>	<b>3</b>
<b>2</b>	<b>Electrostatic accelerators</b>	<b>4</b>
2.1	Voltage breakdown . . . . .	5
2.2	Example: Self-Limited Current in a Planar Diode . . . . .	9
<b>3</b>	<b>Radio-Frequency (RF) accelerators</b>	<b>11</b>
3.1	RF cavities and structures . . . . .	14
3.2	Particle dynamics in RF fields . . . . .	18
3.3	Longitudinal motion in a circular accelerator . . . . .	22
3.4	Bunch distribution . . . . .	23
3.5	Measurement of bunch profiles and reconstruction of the distribution . . . . .	25
<b>4</b>	<b>Transverse Beam Focusing and Transport</b>	<b>26</b>
4.1	Beam Focusing by Quadrupole Magnets . . . . .	26
4.2	Periodic Focusing Channels . . . . .	32
4.3	Emittance, Envelope and Admittance . . . . .	34
4.4	FODO Quadrupole Channel . . . . .	35
4.4.1	Thin elements . . . . .	36
4.4.2	Thick elements . . . . .	37
4.5	Dipole magnets and bending angle . . . . .	41

---

\*see TUCAN for the latest version

<b>5</b>	<b>Synchrotrons</b>	<b>44</b>
5.1	Acceleration in a synchrotron . . . . .	47
5.2	Momentum compaction factor . . . . .	48
5.3	Steering and Focusing Errors . . . . .	49
5.3.1	Chromaticity . . . . .	51
5.4	Restriction of dynamic aperture by sextupoles . . . . .	54
5.5	Vacuum pipes and eddy currents . . . . .	55
<b>6</b>	<b>Beam intensity effects</b>	<b>58</b>
6.1	Transverse intensity effects . . . . .	58
6.1.1	Transverse space charge . . . . .	58
6.1.2	Equation of Motion with Space Charge . . . . .	59
6.1.3	Space Charge Tune Shift . . . . .	62
6.1.4	Nonlinear space charge force . . . . .	62
6.1.5	Beam-beam tune shift . . . . .	63
6.1.6	Image fields and transverse impedances . . . . .	64
6.1.7	Transverse coherent beam oscillations . . . . .	67
6.2	Longitudinal intensity effects . . . . .	69
6.2.1	Field of a relativistic point charge . . . . .	69
6.2.2	Longitudinal space charge . . . . .	70
6.2.3	Synchrotron oscillations with space charge . . . . .	72
6.2.4	Space charge waves and instabilities . . . . .	73

# 1 Prerequisites

The equation of motion for a particle of charge  $q$  moving under the influence of electric and magnetic fields  $\vec{E}$  and  $\vec{B}$  is

$$\frac{d\vec{p}}{dt} = q \left( \vec{E} + \vec{v} \times \vec{B} \right) \quad (1)$$

where  $\vec{p} = \gamma m \vec{v}$  is the momentum,  $\vec{v}$  is the velocity, and  $m$  is the invariant mass.  $\gamma$  is the Lorentz factor:

$$\gamma = \frac{1}{\sqrt{1 - \beta^2}} \quad (2)$$

with the relativistic  $\beta$  parameter  $\beta = v/c$ . When  $\vec{E}$  and  $\vec{B}$  represent static fields that do not depend on time explicitly, we can obtain a first integral of the equation of motion, which can be identified as the total energy  $W$  of the particle. Therefore we first multiply each side of Eq. 1 with  $\vec{v}$  (Remark:  $\vec{v} \perp (\vec{v} \times \vec{B})$ ) and differentiate the left side. Further simplifications (exercise !) yield

$$\frac{d}{dt}(\gamma mc^2) = q \vec{E} \cdot \vec{v} = q \vec{E} \cdot \frac{d\vec{s}}{dt} \quad (3)$$

which can be stated as

$$\frac{d}{dt}(\gamma mc^2 + U) = 0 \quad (4)$$

with the total energy  $W = \gamma mc^2$  and the potential energy

$$U = -q \int \vec{E} \cdot d\vec{s} \quad (5)$$

From Eq. 3 the energy gain due to the applied electric fields in an accelerator can be obtained. Particle energies are given in electron-Volt (eV) or its successive thousandfold multiples (keV, MeV, GeV, TeV). The electron-Volt is the energy of a particle having one electronic unit of charge after it has been accelerated through an electrostatic potential difference of one Volt. So  $1 \text{ eV} = 1.6 \times 10^{-19} \text{ J}$ .

The electric and magnetic fields must satisfy Maxwell's equations. In vacuum, Maxwell's equations in differential form are

$$\nabla \cdot \vec{E} = \frac{\rho}{\epsilon_0} \quad (6)$$

$$\nabla \cdot \vec{B} = 0 \quad (7)$$

$$\nabla \times \vec{E} = -\frac{\partial \vec{B}}{\partial t} \quad (8)$$

$$\nabla \times \vec{B} = \mu_0 \vec{j} + \frac{1}{c^2} \frac{\partial \vec{E}}{\partial t} \quad (9)$$

$$(10)$$

where  $\vec{\rho}$  and  $\vec{j}$  are the charge and current densities respectively. In simple geometries the integral forms are often more convenient than the differential equations. These are

$$\epsilon_0 \int \vec{E} \cdot d\vec{A} = \int \rho dV \quad (11)$$

$$\int \vec{B} \cdot d\vec{A} = 0 \quad (12)$$

$$\oint \vec{E} \cdot d\vec{s} = - \int \frac{\partial \vec{B}}{\partial t} \cdot d\vec{A} \quad (13)$$

$$\oint \vec{B} \cdot d\vec{s} = \mu_0 \int \vec{j} \cdot d\vec{A} + \frac{1}{c^2} \int \frac{\partial \vec{E}}{\partial t} \cdot d\vec{A} \quad (14)$$

The first is Gauss's law, the third is Faraday's law of electromagnetic induction and the fourth is Ampere's law as modified by Maxwell to include the displacement current contribution.

## 2 Electrostatic accelerators

The most common particle accelerator is probably the cathode ray tube shown in Fig. 1, invented by Karl Ferdinand Braun in 1879. Every CRT monitor can be regarded as a primitive particle (electron) accelerator. But according to present convention, the term *particle accelerator* is reserved for devices achieving particle energies of the order of 1 MeV or more. The first accelerator in the modern sense was the electrostatic accelerator designed and used (1932) by Cockcroft and Walton (see Fig. 2). The Cockcroft and Walton accelerator is basically a voltage multiplier that converts AC power from a low voltage level to a higher DC voltage level. It is made up of a voltage multiplier ladder network of capacitors and diodes to generate high voltages. Today Cockcroft-Waltons accelerators are still being used as preaccelerator for proton synchrotron facilities, operating at typically 750 kV (see Fig. 3). The accelerating voltage achievable by a Cockcroft-Walton accelerator is limited by the physical properties of the capacitors and diodes. To obtain higher accelerating voltages a Van de Graaff accelerator is used. The Van de Graaff machine was designed by Robert Jemison Van de Graaff (1901-1967). A continually moving belt of insulating material runs between two pulleys which are separated by an insulated column. The lower pulley is earthed

and attached to the pulley is a sharp metallic comb which is maintained at a potential difference of a few kV between itself and the pulley. A high electric field is produced at the time of the comb and an electrical discharge occurs through the belt from the comb to the pulley, removing electrons from the belt, making it positively charged. The belt carries the charge up to the top pulley which is inside a large ball shaped metal electrode. The electrode then acquires an increasing positive charge with correspondingly high electric potential. The voltage rises rapidly until an equilibrium is established where the rate of loss of negative charge balances the positive charge current carried by the moving belt. In this way, the Van de Graaf machine can reach very high electric potentials of a few 10 MV. In a Van de Graaff accelerator, the high electric potential is coupled to an accelerating tube at the top of which is an ion source that produces the particles to be accelerated. The maximum accelerating potential is limited by breakdown across the accelerating tube and charge leakage from the high voltage electrode. However, with careful design, Van de Graaff accelerators operating at accelerating potentials in excess of 25 MV have been built. A variation of the Van de Graaff accelerator is the tandem accelerator, which can produce accelerating potentials twice as high as that from a single Van de Graaff accelerator. Negative ions are produced which are then accelerated to a certain electrode which forms part of a Van de Graaff machine. The ions are then stripped of two of their electrons and emerge as positive ions, accelerating away from the central electrode towards the target. The ions thus gain kinetic energy twice, once as negative ions and then as positive ions in a tandem fashion. Accelerators of this kind are able to accelerate protons to energies in excess of 40 MeV. The energy capability of electrostatic accelerators has slowly increased, ultimately it is limited by voltage breakdown. In order to reach higher energies time varying electromagnetic fields are required.

## 2.1 Voltage breakdown

In 1889, F. Paschen published a paper (Wied. Ann., 37, 69) which set out what has become known as Paschen's Law. The law essentially states that, at higher pressures (above a few torr) the breakdown characteristics of a gap are a function (generally not linear) of the product of the gas pressure and the gap length, usually written as  $V = f(pd)$ , where  $p$  is the pressure and  $d$  is the gap distance (see also Fig. 5).

$$V(pd) = \frac{Apd}{\ln(pd) + B} \quad (15)$$

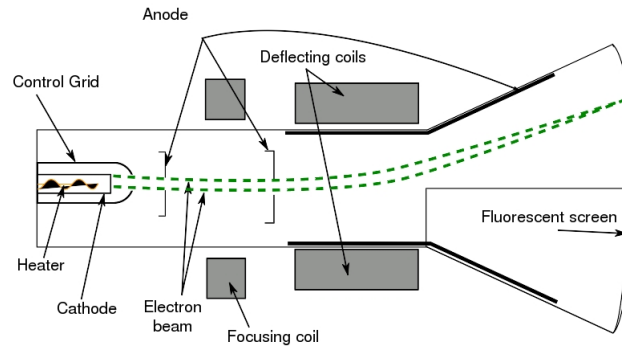


Figure 1: Sketch of a cathode ray tube employing electromagnetic focus and deflection fields.

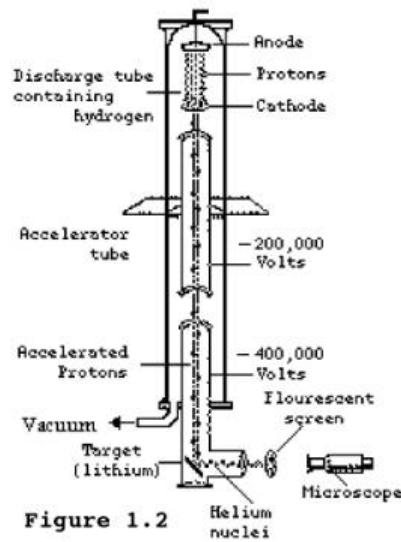


Figure 1.2

Figure 2: Sketch of a Cockcroft-Walton electrostatic accelerator. High voltage is produced by charging capacitors in parallel and discharging them in series.

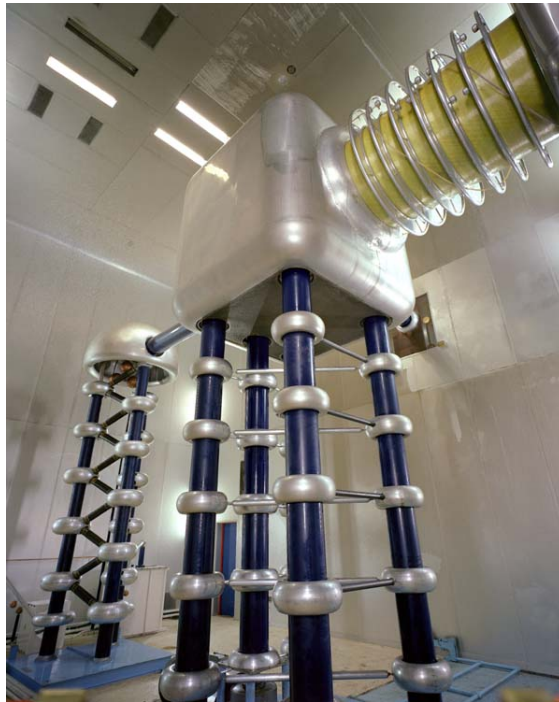


Figure 3: Cockcroft-Walton preaccelerator at the Fermi National Accelerator Laboratory. This device provides negative hydrogen ions at 750 keV kinetic energy for subsequent acceleration through the Fermilab facility.

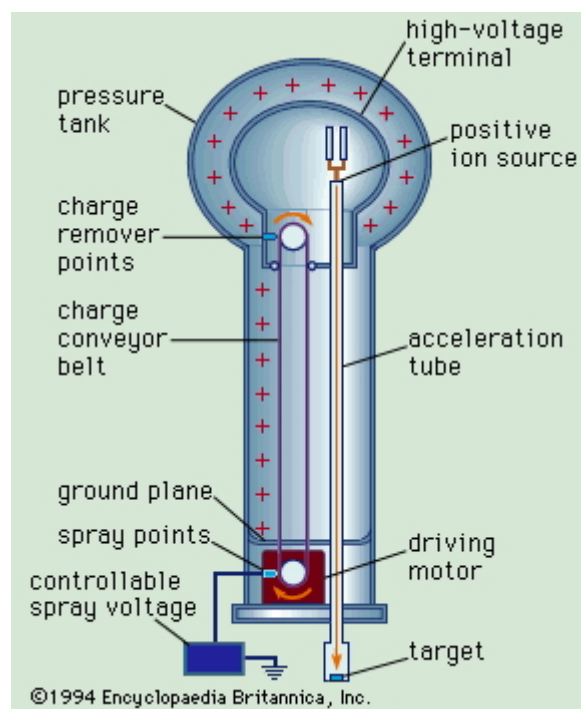


Figure 4: Schematic diagram of a Van de Graaff high-voltage electrostatic generator.



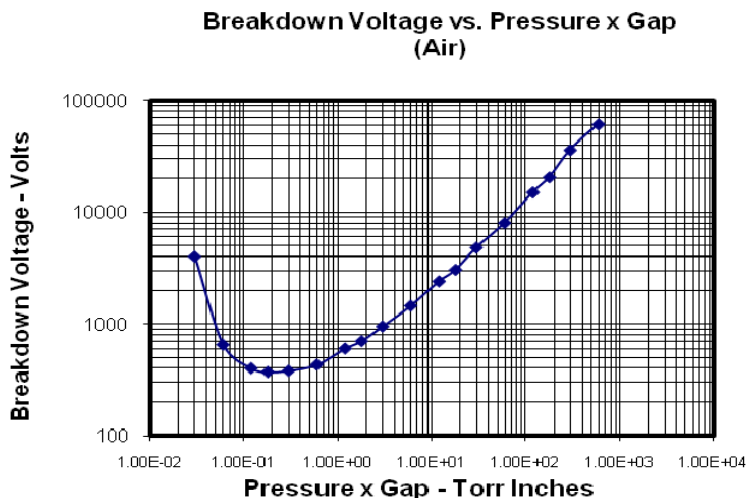


Figure 5: The Paschen Curve for air, two flat parallel copper electrodes, separated by 1 inch (2.54 cm), for pressures between  $3 \cdot 10^{-2}$  torr and 760 torr (1 atm).

The constants  $A$  and  $B$  depend upon the composition of the gas. For dry air the breakdown voltage is approx.  $3 \cdot 10^6$  V/m, such that for a distance of 3 m the breakdown voltage would be 10 MV. In Van de Graaff and tandem accelerators high pressure sulfur hexafluoride (SF6) gas is often used to increase the the threshold of voltage breakdown.

## 2.2 Example: Self-Limited Current in a Planar Diode

As a realistic example for electrostatic acceleration we will treat here the extraction of ions from a source in a planar diode. This example will also illustrate some of the effects arising from the coupling of particles through self-generated fields. A typical ion source with a diode configuration is shown schematically in Fig. 6. The ions are extracted from a plasma, and the accelerated beam passes through a hole of the extraction electrode into the vacuum drift tube. The emitting plasma surface area is not fixed. It has a concave shape, which depends on the plasma density and the strength of the accelerating electric field at the plasma surface. Within a simplified analysis we assume that all ions are launched with initial velocity  $\mathbf{v}_0 = 0$  from a planar anode plasma surface (i.e. they move on straight lines in z-direction). We try to find the steady state solution ( $\partial/\partial t = 0$ ) in a self-consistent form. The electrostatic potential is determined from the beam's charge density  $\rho$

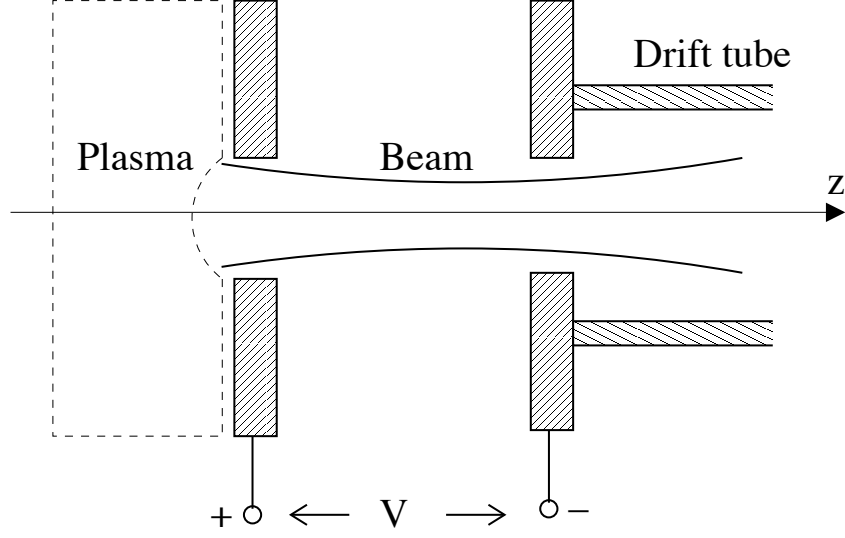


Figure 6: Schematic of a plasma ion source. The ions are emitted from the concave plasma sheath, which forms an equipotential surface.

via Poisson's equation, with  $\phi(z = 0) = 0$  and  $\phi(z = d) = -V_0$ . The relationship between  $\rho$ , the current density  $j_z$  and the ion velocity  $v$  follows from the continuity equation ( $\partial j_z / \partial z = 0$ , or  $j_z = \rho v = \text{const}$ ). The velocity in turn depends on the potential  $\phi$  and is found by integrating the equation of motion. Thus we have three equations:

$$\nabla^2 \phi = \frac{d^2 \phi}{dz^2} = -\frac{\rho}{\epsilon_0} \quad (\text{Poisson's equation}) \quad (16)$$

$$j_z = \rho \dot{z} = \text{const} \quad (\text{continuity equation}) \quad (17)$$

$$\frac{m}{2} \dot{z}^2 = -q\phi(z) \quad (\text{equation of motion}) \quad (18)$$

Substituting  $\phi(z) = -V(z)$  and  $\dot{z} = [2qV(z)/m]^{1/2}$  from (18) into (17) and  $\rho = j_z / \dot{z}$  from (17) into (16) yields

$$\frac{d^2 V}{dz^2} = \frac{j_z}{\epsilon_0 (2q/m)^{1/2}} \frac{1}{V^{1/2}}$$

After multiplication with  $dV/dz$  we can integrate and obtain

$$\left( \frac{dV}{dz} \right)^2 = \frac{4j_z}{\epsilon_0 (2q/m)^{1/2}} V^{1/2} + C$$

For  $V(z=0) = 0$  together with  $dV/dz = 0$  at  $z = 0$  we obtain  $C = 0$ . A second integration then yields

$$\frac{4}{3}V^{3/4} = 2 \left( \frac{j_z}{\epsilon_0} \right)^{1/2} \left( \frac{2q}{m} \right)^{-1/4} z$$

and with  $V(z=d) = V_0$

$$V(z) = V_0 \left( \frac{z}{d} \right)^{4/3}$$

with the relation

$$j_z = \frac{4}{9}\epsilon_0 \left( \frac{2q}{m} \right)^{1/2} \frac{V_0^{3/2}}{d^2} \quad [\text{A/m}^2]$$

This equation is known as *Child-Langmuir law*\* Applying this result to a uniform round beam extracted from emitted from a circular area with radius  $r_s$  yields for the *space charge limited beam current*

$$I = \frac{4\pi}{9}\epsilon_0 \left( \frac{2q}{m} \right)^{1/2} \frac{V_0^{3/2} r_s^2}{d^2} \quad [\text{A}] \quad (19)$$

However, in practical ion sources with cylindrical geometry the beam current may be considerably lower than this limit, which is based on an ideal one-dimensional planar diode geometry. In high current ion sources the achievable beam current is often limited by high-voltage breakdown.

### 3 Radio-Frequency (RF) accelerators

The term linear accelerator (linac) is reserved for an accelerator in which charged particles move on a linear path and are accelerated by time-dependent electromagnetic fields. The first RF linear accelerator was demonstrated experimentally by Wideröe in 1927 at Aachen.

The Wideröe linac concept, shown in Fig. 7, was to apply a time-alternating voltage to a sequence of drift tubes whose length increased with increasing particle velocity, so that the particles arrive at every gap at the right time to be accelerated. The length of the  $i$ -th drift tube is

$$l_i = \frac{1}{2} v_i T_{\text{rf}} \quad (20)$$

---

\* C.D. Child, Phys. Rev. Ser. I **32**, 492 (1911); I. Langmuir, Phys. Rev. Ser. II **2**, 450 (1911)

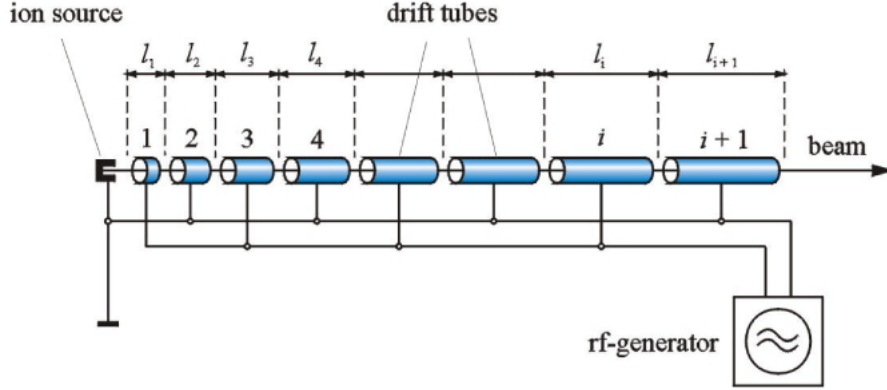


Figure 7: Concept of the Wideroe linear accelerator.

with the velocity  $v_i$  in the gap and the period of the rf generator  $T_{\text{rf}}$ . The non-relativistic particle energy  $W_s$  in the  $i$ -th drift tube is

$$(W_s)_i = \frac{1}{2}mv_j^2 \quad (21)$$

and the energy gain in the gap is

$$(W_s)_{i+1} = (W_s)_i + qV_0 \sin \phi_s \quad (22)$$

with the rf phase  $\phi_s$  and the rf voltage amplitude  $V_0$ . The length of the  $i$ -th drift tube results as

$$l_j = \frac{T_{\text{rf}}}{2} \sqrt{\frac{2}{m} (W_{s0} + jqV_0 \sin \phi_s)} \quad (23)$$

with the initial particle energy  $W_{s0}$ . The injection energy is usually small. Therefore the length of the drift tubes increases with the square root of the gap number. From the equations above it becomes clear that the rf frequency determines the length of rf accelerator structures.

Fig. 8 shows the old Wideröe structure used at GSI for the acceleration of protons and heavy ions up to an energy of 1.4 MeV/u. The structure was operated at 27 MHz. In 1999 the Wideröe was replaced by a more effective injector.

For larger particle energies the Wideröe concept is not suitable. The length of the drift tubes would be impractically large, unless the frequency could be increased. However, at larger frequencies electromagnetic wave propagation and radiation effects must be included.

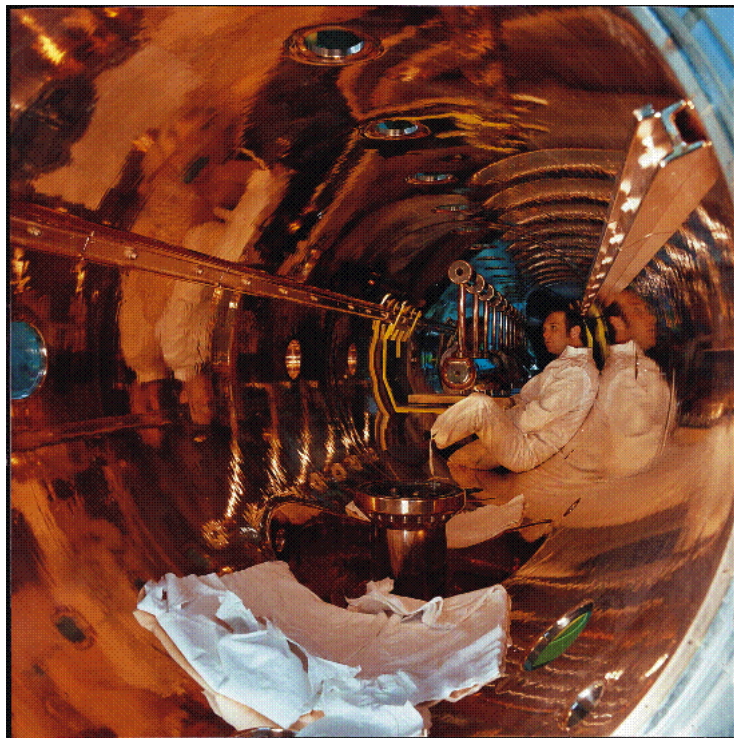


Figure 8: Wideröe structure used at GSI.

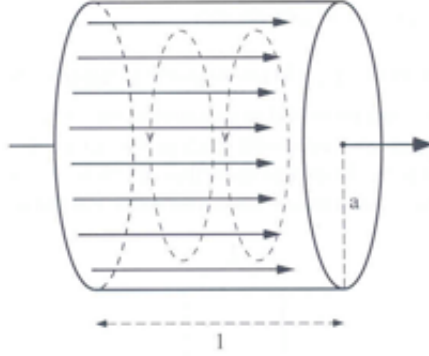


Figure 9: A pillbox cavity of radius  $a$  and length  $l$ . The electric (solid lines) and magnetic (broken lines) field vectors are indicated for the lowest frequency mode.

### 3.1 RF cavities and structures

In order to accelerate particles to high energies one excites electromagnetic modes in cavity-like structures. The basic accelerating structure is often referred to as a *resonant cavity*. A linear accelerator can be regarded as a sequence of such resonant cavities, through which the particles make a single passage in order to achieve their final energy. A circular accelerator usually has one or more cavities through which the particles pass repetitively.

A basic resonant cavity might look like the cylindrical object depicted in Fig. 9, called pillbox cavity. We want a mode with an accelerating field  $E_z$ , where  $z$  is in the direction of the particle motion. If we assume that  $E_z$  and  $B_\theta$  are the only electric and magnetic field components, Maxwell's equations reduce to

$$\frac{1}{r} \frac{\partial}{\partial r} (r B_\theta) = \frac{1}{c^2} \frac{\partial E_z}{\partial t} \quad (24)$$

$$\frac{\partial E_z}{\partial r} = \frac{\partial B_\theta}{\partial t} \quad (25)$$

After eliminating  $B_\theta$  we obtain

$$\frac{\partial^2 E_z}{\partial r^2} + \frac{1}{r} \frac{\partial E_z}{\partial r} = \frac{1}{c^2} \frac{\partial^2 E_z}{\partial t^2} \quad (26)$$

A mode with angular frequency  $\omega$  will have a solution of the form

$$E_z(r, t) = E(r) e^{i\omega t}. \quad (27)$$

Therefore

$$E'' + \frac{E'}{r} + \left(\frac{\omega}{c}\right)^2 E = 0 \quad (28)$$

This is Bessel's equation of zero order, so the solution is

$$E(r) = E_0 J_0 \left( \frac{\omega}{c} r \right). \quad (29)$$

At  $r = a$  the field must vanish if the cavity material is a good conductor. The argument of the Bessel function must then be one off the zeros of  $J_0$ , and the lowest frequency mode will be associated with the first zero

$$\frac{2\pi f}{c} a = 2.405. \quad (30)$$

With  $a \approx 30$  cm  $f$  is in the 400 MHz range, which is an appropriate frequency for radio-frequency power sources.

Next we want to calculate the energy gain of a particle passing the cavity. Therefore we assume a longitudinal electric field in the cavity, that is independent on the longitudinal coordinate  $z$

$$E_z(t) = \hat{E}_z \cos(\omega_{\text{rf}} t) \quad (31)$$

If a particle passes through the cavity with the velocity  $v$ , its coordinate is  $z = vt$ . The total energy gain along the cavity length  $l$  is

$$\Delta W = \int_0^l q \hat{E}_z \cos(\omega_{\text{rf}} z/v) dz = q V_0 \frac{\sin \theta}{\theta} \quad (32)$$

with

$$\theta = \frac{\omega_{\text{rf}} l}{v} \quad (33)$$

if we substitute  $\hat{E}_z$  through the the voltage amplitude  $V_0$  in the cavity divided by the cavity length  $l$ . The energy gain can now be written as

$$\Delta W = q V_0 T \quad (34)$$

with the transit time factor

$$T = \frac{\sin \theta}{\theta} \quad (35)$$

The transit time factor should be close to unity. As an example we can calculate the maximum length of a pillbox cavity in order to obtain a transit

time factor  $T > 0.9$  corresponding to  $\theta \lesssim 0.8$ . For  $v = c$  and using Eq. (30) for the lowest mode frequency in the cavity yields

$$\theta = 2.405 \frac{l}{a} \quad (36)$$

For the example cavity radius  $a = 30$  cm one obtains the maximum length  $l = 10$  cm.

Next we want to calculate the losses due to ohmic heating in the cavity wall. From Ampere's law the surface current density is related to the magnetic field according to

$$J = \frac{1}{\mu_0} B_\phi \quad (37)$$

where  $J$  is parallel to the axes on the inner surface of the cylinder. From

$$B_\phi = \frac{E_0}{c} J_1 \left( \frac{\omega}{c} r \right). \quad (38)$$

we can obtain the loss rate by integration of  $\rho_s J^2/2$  over the cavity surface.  $\rho_s$  is the surface resistivity of the wall and the factor 1/2 arises from averaging over one cycle. The surface resistivity is the resistivity of the bulk material divided by the skin length. The power loss rate is (exercise)

$$P = \frac{1}{2} \rho_s \left( \frac{E_0}{\mu_0 c} \right)^2 2\pi a l \left( 1 + \frac{a}{l} \right) J_1^2(2.405) \quad (39)$$

One figure of merit for a cavity design is the shunt impedance  $R_s$  defined as

$$R_s = \frac{(\text{energy gain per unit charge})^2}{P} \quad (40)$$

The shunt impedance gives a measure of how much voltage  $V_0$  one can get with a given power  $P$ , which is dissipated in the cavity walls. For the pillbox cavity the shunt impedance is

$$R_s = \frac{Z_0^2 l}{\pi \rho_s a} \frac{T^2}{(1 + (a/l)) J_1^2(2.405)} \quad (41)$$

where  $Z_0$  is the vacuum impedance  $(\mu_0/\epsilon_0)^{1/2}$ . The quality factor  $Q$  is another important parameter. It is defined as the ratio of the stored energy  $U$  to the energy lost in one radian of an oscillation and describes the bandwidth  $\Delta\omega$  of the cavity

$$Q = \frac{\omega U}{P} = \frac{\omega}{\Delta\omega} \quad (42)$$



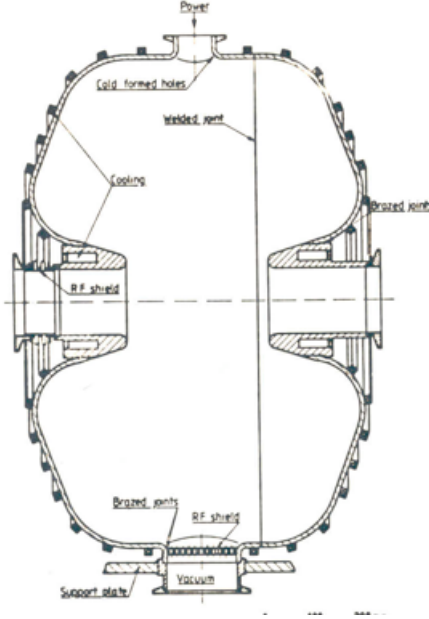


Figure 10: A pillbox cavity with a nose-cone in order to concentrate the electric field around the axis. In addition the cavity has a spherical shape in order to spread the surface currents.

The stored energy can be calculated from the electric field alone

$$U = \frac{1}{2}\epsilon_0 \int E^2 dV = \frac{1}{2}\epsilon_0 E_0^2 V J_1^2(2.405) \quad (43)$$

and the quality factor results as

$$Q = \frac{2.405\mu_0 c}{2\rho_s(1 + (a/l))} \quad (44)$$

Many changes to the pillbox cavity design can improve its performance. For example one could add a nose cone to concentrate the electric field around the axis or one could use a spherical shape in order to spread the surface currents and to lower the ohmic losses in the wall (see Fig. 10).

The design of rf cavities for accelerators is a very complex field. Here we just would like to notice that for the acceleration of low energy particles, with a relativistic parameter  $\beta < 1$  in circular ion accelerators, as we will later see, it is necessary to significantly vary the rf frequency of the cavities. Cavities for this purpose are filled with a material of relative permeability  $K_m = \mu/\mu_0$ . The resonant frequency of the cavity will be reduced by the

factor  $1/\sqrt{K_m}$ . This can be easily seen by noting that Eq. 24 will now contain  $K_m$  on the right hand side. The  $\mu$  of the material can be tuned e.g. by a static external magnetic field.

A single cavity is usually not sufficient to provide the required energy gain in a synchrotron and surely not in a linear accelerator (linacs). Especially in linacs arrays of cavities are grouped in a to form multicell resonator structures.

### 3.2 Particle dynamics in RF fields

In this section we will analyze the acceleration of particles by a sequence of equidistant rf cavities. The energy gain of the ideal or design particle with energy  $W_0 = m\gamma_s c^2$  in an individual cavity or acceleration gap is

$$\Delta W = qV_0 \cos \phi_s \quad (45)$$

with the phase  $\phi_s$  at which the ideal particle enters the cavity. Now we can construct the equations governing the motion of a particle of arbitrary energy and phase. Suppose a particle leaves the  $n$ th cavity with energy  $W_n$  and phase  $\phi_n$  as shown in Fig. 11.

The time needed to arrive at the next cavity is  $t_{n+1} = d/(\beta_{n+1}c)$ , with the particle velocity  $\beta_{n+1}c$  and the distance  $d$  between the cavities. Let  $\Delta t_{n+1} = t_{n+1} - t_s$  be the time difference between the arbitrary particle and the ideal particle. Then at the entrance to this  $(n+1)$ st cavity the phase difference would be

$$\begin{aligned} \phi_{n+1} &= \phi_n + \omega_{rf} \Delta t_{n+1} \\ &= \phi_n - \frac{\omega_{rf} d}{\beta_0 c} \left( \frac{\Delta \beta}{\beta} \right)_{n+1} \\ &= \phi_n - \frac{\omega_{rf} d}{\beta_0^3 \gamma_0^2 c} \left( \frac{\Delta W}{W_0} \right)_{n+1}. \end{aligned} \quad (46)$$

where we used

$$\Delta t = -\frac{d}{\beta c} \frac{\Delta \beta}{\beta} \quad (47)$$

and

$$\frac{\Delta \beta}{\beta} = \frac{1}{\beta^2 \gamma^2} \frac{\Delta W}{W} \quad (48)$$

that can be obtained by differentiation of  $W = m\gamma c^2$  with  $\gamma = 1/(1 - \beta^2)$ . The ideal particle always arrives at the stations at the same phase  $\phi_s$ . We will assume, that the distance between cavities is adjusted to the ideal particle as  $d = \beta_0 \lambda_{rf}$ , with the rf wave length  $\lambda_{rf} = 2\pi c/\omega_{rf}$ .

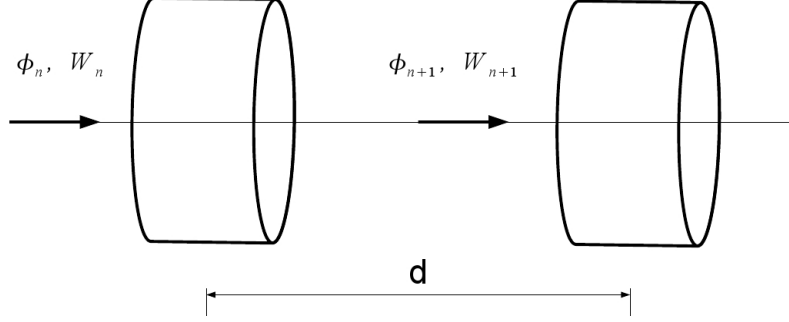


Figure 11: A particle enters the  $n$ th accelerating station with energy  $E_n = W_n$  and phase  $\phi_n$ .

The second difference equation treats the step in energy in passage through the cavity. If  $(W_0)_n$  is the energy of the ideal particle at the entrance to the  $n$ th cavity, then

$$(W_0)_{n+1} = (W_0)_n + qV_0 \cos \phi_s \quad (49)$$

For a general particle the corresponding equation will be

$$W_{n+1} = W_n + qV_0 \cos \phi_n \quad (50)$$

and so the difference in energy between the particle in question and the ideal particle,  $\Delta W = W - W_0$ , must satisfy

$$\Delta W_{n+1} = \Delta W_n + qV_0(\cos \phi_n - \cos \phi_s) \quad (51)$$

Eq. 51 together with the difference equation for the phase

$$\phi_{n+1} = \phi_n - \frac{2\pi}{\beta_0^2 \gamma_0^2} \left( \frac{\Delta W}{W_0} \right)_{n+1} \quad (52)$$

describe the motion of a particle with respect to the ideal particle.

For the further analytic studies we approximate the difference equation by differential equations. This can be justified by small relative changes of

phase and energy between two cavities. We may thus relate the cavity index  $n$  to the independent variable distance  $s = nd = n\beta_0\lambda_{rf}$  and rewrite the difference equations as

$$\frac{d\phi}{ds} = -\frac{2\pi}{\beta_s^3\gamma_s^2\lambda_{rf}} \left( \frac{\Delta W}{W_s} \right) \quad (53)$$

$$\frac{d\Delta W}{ds} = \frac{qV_0}{\beta_s\lambda_{rf}} (\cos\phi - \cos\phi_s) \quad (54)$$

These two first order differential equations may be turned into a single second order equation

$$\frac{d^2\phi}{ds^2} = -\frac{2\pi qV_0}{\beta_s^4\gamma_s^2\lambda_{rf}^2 W_s} (\cos\phi - \cos\phi_s) \quad (55)$$

A first integral can be obtained multiplying by  $d\phi/ds$  and integrating over  $s$ :

$$\frac{1}{2} \left( \frac{d\phi}{ds} \right)^2 - \frac{2\pi qV_0}{\beta_0^4\gamma_0^2\lambda_{rf}^2 W_0} (\sin\phi + \phi \cos\phi_s) = \text{constant}. \quad (56)$$

The term on the lhs of the above equation can be regarded as the kinetic energy and the potential energy of a nonlinear oscillator. The constant on the rhs is the total energy. The particles that are trapped inside this potential form a *bunch*. The area of the potential that provides stable oscillations is called *rf bucket* (see also Fig. 12). Combining Eqs. 53 and 56, we find the expressions for contours describing particle motion in  $\phi - \Delta W$  space:

$$\Delta W^2 - \frac{\beta_0^2\gamma_0^2 W_0 q V}{\pi} (\sin\phi + \phi \cos\phi_s) = \text{constant}. \quad (57)$$

In order to obtain a simple expression for the frequency of phase oscillations it is convenient to linearize the equation of motion Eq. 55. We assume that  $\Delta\phi = \phi - \phi_s$  is small

$$\cos(\phi_s + \Delta\phi) - \cos\phi_s \approx -\sin\phi_s \Delta\phi \quad (58)$$

Eq. 55 can now be written as

$$\frac{d^2\Delta\phi}{ds^2} = -\frac{\omega_s^2}{\beta_0^2 c^2} \Delta\phi \quad (59)$$

with the *synchrotron frequency* for small amplitude oscillations:

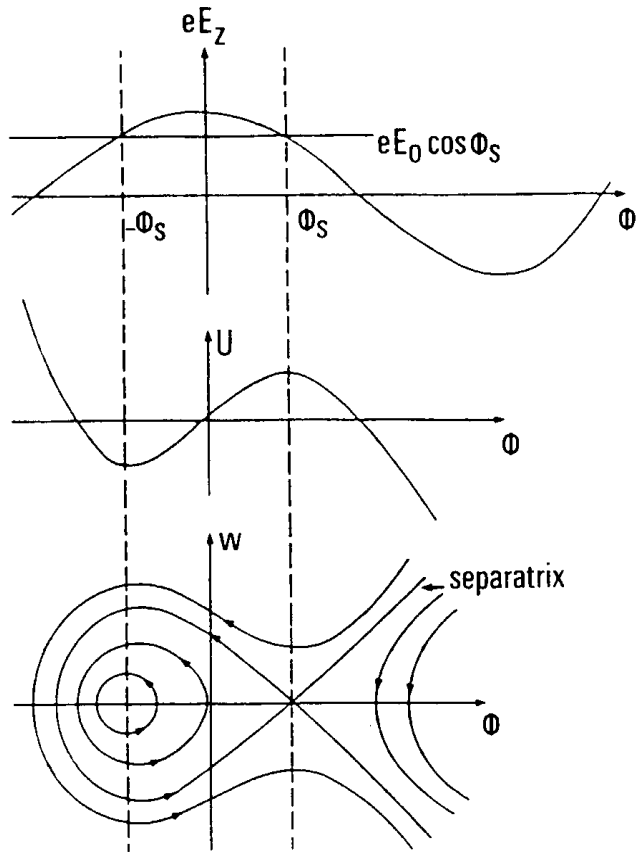


Figure 12: Phase stability curves. The closed particle trajectories in the lower Figure correspond to stable synchrotron oscillations in the rf bucket. The outermost stable trajectory is the separatrix or bucket boundary.

$$\omega_s = \sqrt{-\frac{2\pi qV \sin \phi_s}{\beta_0^2 \gamma_0^3 \lambda_{rf}^2 m}} \quad (60)$$

From the above expression for the synchrotron frequency we see that  $\phi_s$  needs to be in the range  $(-\pi/2, 0)$  in order to obtain stable oscillations.

From Eq. 59 we obtain the solution for the small amplitude phase oscillations

$$\Delta\phi = \hat{\phi} \cos(k_s s + \chi) \quad (61)$$

with the oscillation wave number  $k_s = \omega_s/(\beta_0 c)$ , the amplitude  $\hat{\phi}$  and an arbitrary phase  $\chi$ . The corresponding oscillations in  $\Delta W$  are given through

$$\Delta W = -\frac{qV \sin \phi_s}{2\pi\nu_s} \hat{\phi} \sin(k_s s + \chi) \quad (62)$$

where we introduced the ratio  $nu_s = \omega_s/\omega_{rf}$ . The particles move along a ellipse in the  $\phi - \Delta W$  phase space. With Eqs. 61 and 62 the phase space ellipse of a particle becomes

$$\left(\frac{\Delta W}{\hat{W}}\right)^2 + \left(\frac{\Delta\phi}{\hat{\phi}}\right)^2 = 1 \quad (63)$$

with the phase space area  $\pi\hat{W}\hat{\phi}$  occupied by the particle. The phase space area enclosed by the ellipse is

$$A = \pi\hat{W}\hat{\phi} \quad (64)$$

The area enclosed by the separatrix (the bucket area)  $A_B$  can be obtained from

$$A_B = 2 \int_0^{2\pi} \Delta W(\phi) d\phi \quad (65)$$

with  $\Delta W$  from Eq. 57.

### 3.3 Longitudinal motion in a circular accelerator

Let  $T$  be the time needed for one ring revolution for the ideal particle. In terms of the ring circumference  $C$  and the particle speed  $v$ ,

$$T = C/v \quad (66)$$

The fractional change in  $T$  associated with deviations in  $L$  or  $v$  is

$$\frac{\Delta T}{T} = \frac{\Delta C}{C} - \frac{\Delta v}{v} \quad (67)$$

The second term can be expressed in terms of the fractional momentum deviation by

$$\frac{\Delta v}{v} = \frac{1}{\gamma^2} \frac{\Delta p}{p} \quad (68)$$

The first term described the change in the path length due to a momentum deviation. This relationship will be derived later in the Section on transverse dynamics (Eq. 133). Here we introduce the parameter  $\gamma_t$  as a proportionality constant

$$\frac{\Delta C}{C} = \frac{1}{\gamma_t^2} \frac{\Delta p}{p} \quad (69)$$

The expression for the fractional change in  $T$  is thus simplified by introducing the parameter

$$\eta = \frac{1}{\gamma_t^2} - \frac{1}{\gamma^2} \quad (70)$$

Notice that at a particular energy  $\gamma = \gamma_t$  the *slip factor*  $\eta$  changes sign. This is called *transition energy*, hence the subscript  $t$ .

The longitudinal equation of motion obtained in Sec. 3.2 for linear accelerators can be easily modified for circular accelerators. In Eq. 46 we have to use  $\Delta t = T(\Delta T/T)$ ,  $d = C$  and  $\omega_{rf}T = 2\pi h$ . Here  $h$  is an integer called the *harmonic number*. With these corrections the synchrotron frequency in a circular accelerator results as (example)

$$\omega_s = \sqrt{-\frac{2\pi h q V \sin \phi_s}{C^2 m^*}} \quad (71)$$

with the *effective mass*  $m^* = -\gamma m/\eta$ . It is important to notice that at transition energy the phase  $\phi_s$  of the rf cavities has to jump by  $\pi$ . Crossing transition energy is always connected with beam quality degradation. Therefore one tries to avoid transitions crossing by either moving  $\gamma_t$  to high values or by injection into a larger ring.

### 3.4 Bunch distribution

The particles of a bunch populate a region in phase space  $\phi - \Delta W$ . The corresponding bunch distribution function is defined as

$$f(\Delta\phi, \Delta W) = \frac{dN}{d(\Delta\phi)d(\Delta W)} \quad (72)$$

here  $dN$  is the number of particles in an infinitesimal phase space element. The bunch density or bunch profile is defined as

$$\rho(\Delta\phi) = \frac{dN}{d(\Delta\phi)} \quad (73)$$

We speak of a *matched bunch distribution* if the distribution does not change with time

$$\frac{df(\phi, \Delta W)}{dt} = 0 \quad (74)$$

This is always the case if the distribution is a function of a time invariant parameter, like e.g. the 'Hamiltonian' or energy of a particle

$$H = \frac{\dot{\phi}^2}{2} - \omega_s^2 \sin \phi \quad (75)$$

where we assumed a stationary, non-accelerating bucket. If we furthermore assume  $\Delta\phi = \phi - \phi_s \ll 1$  we obtain

$$H = \frac{\dot{\phi}^2}{2} + \frac{1}{2}\omega_s^2(\Delta\phi)^2 \quad (76)$$

The particle with the maximum amplitude  $\phi_m$  in the bunch determines the boundary of the distribution with  $H = H_m$

$$H_m = \frac{1}{2}\omega_{s0}^2\phi_m^2 \quad (77)$$

An example of a matched bunch distribution is the elliptic bunch distribution

$$f(H) = \sqrt{H - H_m} = A \sqrt{1 - \left(\frac{\Delta W}{W_m}\right)^2 - \left(\frac{\Delta\phi}{\phi_m}\right)^2} \quad (78)$$

The bunch area for this distribution is given by the bunch boundary ellipse

$$A = \pi W_m \phi_m \quad (79)$$

The elliptic bunch distribution yields to a parabolic bunch density

$$\rho(\Delta\phi) = \int_{-W_m}^{W_m} f(\Delta W, \phi) d(\Delta W) = \rho_m \left(1 - \left(\frac{\Delta\phi}{\phi_m}\right)^2\right) \quad (80)$$

with the peak density in the bunch center  $\rho_m$ . Another important example is the Boltzmann distribution

$$f(H) = A \exp\left(-\frac{H}{H_m}\right) = A \exp\left(-\frac{(\Delta W)^2}{2\sigma_W^2}\right) \exp\left(-\frac{(\Delta\phi)^2}{2\sigma_\phi^2}\right) \quad (81)$$



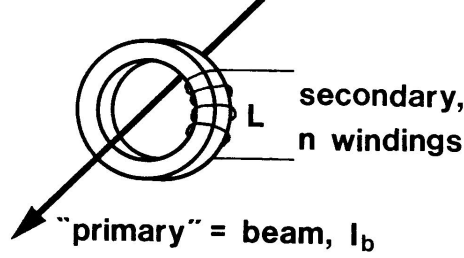


Figure 13: Principle of a beam current transformer.

with the bunch density

$$\rho(\Delta\phi) = \rho_m \exp\left(-\frac{(\Delta\phi)^2}{2\sigma_\phi^2}\right) \quad (82)$$

and the rms bunch length

$$\sigma_\phi^2 = \frac{\int_0^{\phi_m} \Delta\phi^2 \rho(\Delta\phi) d(\Delta\phi)}{\int_0^{\phi_m} \rho(\Delta\phi) d(\Delta\phi)} \quad (83)$$

For a Boltzmann distribution we can define a rms bunch area  $A = \pi\sigma_\phi\sigma_W$ . It is important to note that during slow (adiabatic) acceleration  $A$  is not constant, but varies according to  $A \sim \beta_0$ . During the acceleration process the extension of a bunch in  $\Delta\phi$  (bunch length) will decrease. This fact is called *adiabatic damping*.

### 3.5 Measurement of bunch profiles and reconstruction of the distribution

The beam current as a function of time  $t$  at a fixed position in the accelerator is

$$I(t) = q\beta_0 c \rho\left(\phi = -\frac{2\pi}{\lambda_{rf}}\beta_0 ct\right) \quad (84)$$

A widely used device for the measurement of beam currents in accelerators is the beam transformer. Figure 13 shows the principle.

An idealized transformer with a secondary winding of inductance  $L$  would result in a voltage  $V = LdI_b/dt$ , with the beam current  $I_b$ , which is not very practical as the current is differentiated. In reality the secondary winding has a capacity  $C$  and is terminated with a resistance  $R$  (see Fig. 14). In this

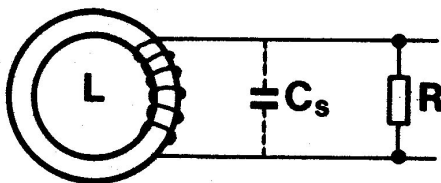


Figure 14: Transformer with capacity  $C$  and termination  $R$ .

case the obtained signal shows a more useful behavior, proportional to the bunch form. Provided that the bunch is longer than the rise time ( $\sim \sqrt{LC}$ ) of the transformer and shorter than its drop time ( $\sim L/R$ ).

Other devices used to measure bunch profiles in accelerators are wall-current monitors and pickups (see e.g. <http://cas.web.cern.ch/cas/Loutraki-Proc/PDF-files/E-Kozioł/DB-Kozioł.pdf>). From the measured bunch profile  $\rho(\phi, t)$  one can reconstruct the bunch distribution using tomographic algorithms (see <http://tomograp.home.cern.ch/tomograp/>). Fig. 15 shows a tomographic reconstruction of the phase space area occupied by a bunch in the CERN proton synchrotron booster (PS Booster) shortly after injection from the linac. The dashed line is the bucket separatrix in the absence of self-fields. The color scale shows the density distribution inside the bunch.

## 4 Transverse Beam Focusing and Transport

In the previous sections we focused on acceleration and longitudinal stability. The task in this and in the following sections is to investigate transverse stability (see Fig. 16).

### 4.1 Beam Focusing by Quadrupole Magnets

Accelerators can not be operated without transverse focusing. For transverse focusing in high energy accelerators magnetic fields are employed. In the absence of currents, magnetic field gradients that provide restoring forces in both transverse degrees of freedom are not possible. The condition  $\vec{\nabla} \times \vec{B} = 0$  leads to

$$\frac{\partial B_y}{\partial x} = \frac{\partial B_x}{\partial y} \quad (85)$$

with the transverse coordinates  $x$  and  $y$  (see Fig. 16). For small displacements,  $x$  and  $y$ , from the ideal trajectory, the field can be written as

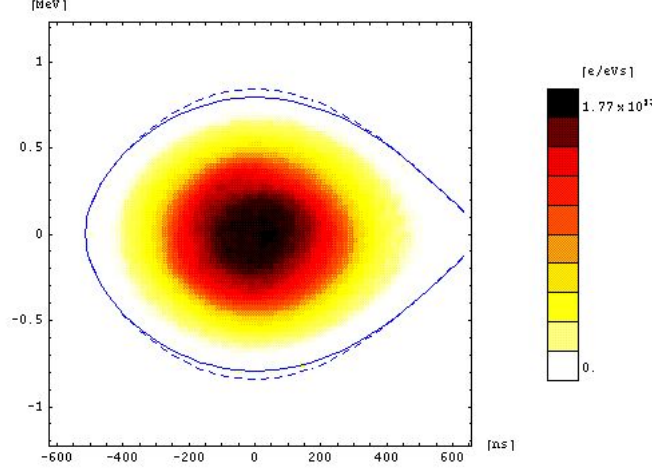


Figure 15: 'Tomographic' reconstruction of the phase space area occupied by a bunch in the CERN proton synchrotron booster (PS Booster). shortly after injection from the linac. The dashed line is the bucket separatrix in the absence of self-fields.

$$\begin{aligned} \vec{B} &= B_x \vec{e}_x + B_y \vec{e}_y \\ &= \left( B_x(0,0) + \frac{\partial B_x}{\partial y} y + \frac{\partial B_x}{\partial x} x \right) \vec{e}_x + \left( B_y(0,0) + \frac{\partial B_y}{\partial y} y + \frac{\partial B_y}{\partial x} x \right) \vec{e}_y \end{aligned} \quad (86)$$

with the unit vectors  $\vec{e}_x$  and  $\vec{e}_y$ . The last term in each component produces a force at right angles to the displacement and hence cannot represent a restoring force. The remaining coefficients of  $x$  and  $y$  are equal according to Eq. 86. Therefore the Lorentz force is focusing in one coordinate and defocusing in the other. The standard magnet that produces this focusing character is the quadrupole.

A magnetic quadrupole field is described through

$$B_y = B_0 \frac{x}{a}, \quad B_x = B_0 \frac{y}{a} \quad (87)$$

Such a field is produced by a magnet configuration with hyperbolic pole shapes, as shown in Figs. 17 and 18. The focusing strength for a magnetic quadrupole is defined as

$$\kappa = \frac{q}{p_0} \frac{\partial B_x}{\partial y} = \frac{q B_0}{\gamma m a v_s} \quad (88)$$

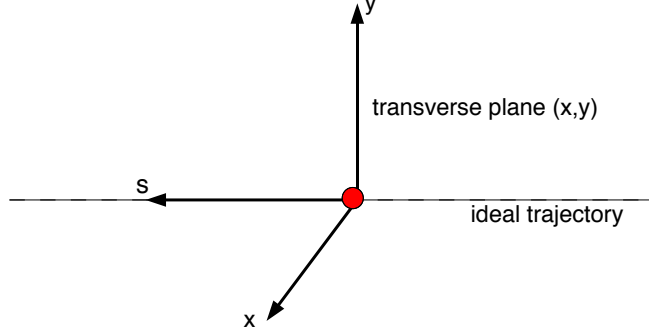


Figure 16: Transverse and longitudinal degrees-of-freedom of particle motion.

for electric quadrupole one obtains

$$\kappa = \frac{qE_0}{\gamma m a v_s^2}.$$

In high energy circular accelerators the bending and focusing forces are produced by magnetic rather than electric fields. For slow, nonrelativistic particles electric fields are more efficient. For a relativistic particle with  $v_0 = c$  we obtain  $\kappa_E/\kappa_M = E_0/(cB_0)$ . In order to provide the equivalent focusing strength of  $B_0 = 1$  T one needs an electric field of 300 MV/m. While the former field strength is typical of magnet devices, the latter is outside of our present reach.

From  $\dot{p}_x = F_x$  and  $\dot{p}_y = F_y$ , with the Lorentz force  $\vec{F}$  one can obtain the transverse equation of motion as

$$x''(s) + \kappa(s)x = 0 \tag{89}$$

$$y''(s) - \kappa(s)y = 0$$

here we use the variable  $s = \beta_0 ct$  instead of  $t$  and we allow the focusing strength to depend on  $s$ . Within a quadrupole magnet  $\kappa$  is normally a constant (see Fig. 19). A general solution for Eq. 89 for constant  $\kappa > 0$  is

$$x(s) = A \cos(\sqrt{\kappa}s) + B \sin(\sqrt{\kappa}s) \tag{90}$$

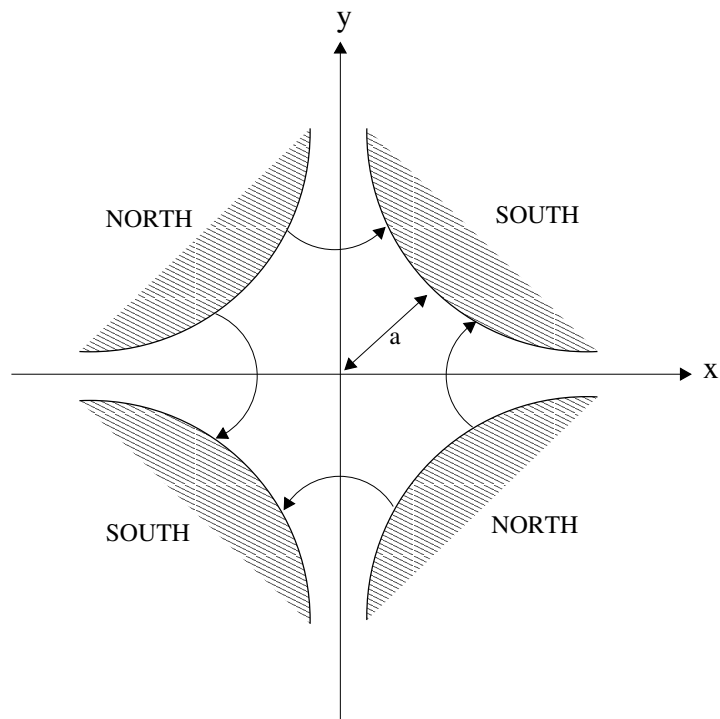


Figure 17: Field lines in a magnetic quadrupole. For an ion moving in the  $s$ -direction, the force components are focusing in the  $x$ -direction and defocusing in the  $y$ -direction.

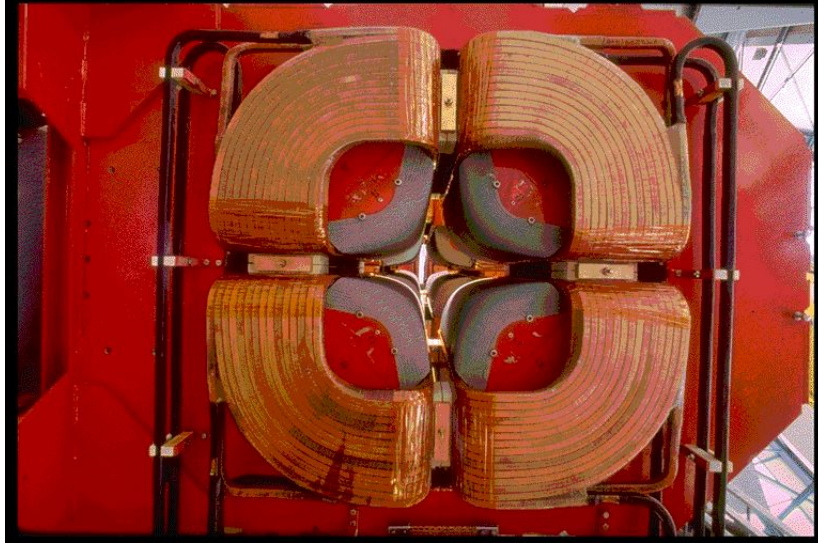


Figure 18: One of the quadrupoles in the GSI heavy ion storage ring ESR.

and for  $\kappa < 0$

$$x(s) = A \cosh(\sqrt{|\kappa|}s) + B \sinh(\sqrt{|\kappa|}s) \quad (91)$$

with coefficients  $A$  and  $B$  that depend on the initial values  $x_0$  and  $x'_0$ .

We can write the solution of Eqs. 89 in matrix form as

$$\begin{pmatrix} x \\ x' \end{pmatrix} = M \begin{pmatrix} x_0 \\ x'_0 \end{pmatrix}$$

where  $x_0$  and  $x'_0$  are the initial coordinates and  $x$  and  $x'$  are the final values. The  $2 \times 2$  matrix  $M$  is called a *transfer matrix*. A beam transport structure usually consists of a sequence of magnets and field-free drift space. For building beam transport lines we are interested in quadrupole magnets that give transverse focusing when  $\kappa > 0$  and defocusing when  $\kappa < 0$ . Furthermore we have field-free drift spaces with  $\kappa = 0$ . Assuming force functions  $\kappa(s)$ , which are piecewise constant inside the elements and change step-like at the element boundaries, we can obtain the following results for the corresponding transfer matrices

*Focusing quadrupole* ( $\kappa > 0$ ) of length  $l$ :

$$M_F = \begin{pmatrix} \cos \sqrt{\kappa}l & \frac{\sin \sqrt{\kappa}l}{\sqrt{\kappa}} \\ -\sqrt{\kappa} \sin \sqrt{\kappa}l & \cos \sqrt{\kappa}l \end{pmatrix} \quad (92)$$

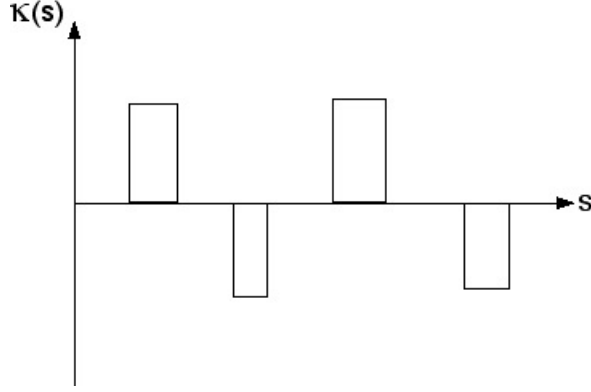


Figure 19: The focusing constant  $\kappa$  varies with position  $s$ , but is normally constant within individual elements of the accelerator.

*Defocusing quadrupole* ( $\kappa < 0$ ) of length  $l$ :

$$M_D = \begin{pmatrix} \cosh \sqrt{|\kappa|}l & \frac{\sinh \sqrt{|\kappa|}l}{\sqrt{|\kappa|}} \\ \sqrt{|\kappa|} \sinh \sqrt{|\kappa|}l & \cosh \sqrt{|\kappa|}l \end{pmatrix} \quad (93)$$

*Drift space* ( $\kappa = 0$ ) of length  $l$ :

$$M_O = \begin{pmatrix} 1 & l \\ 0 & 1 \end{pmatrix} \quad (94)$$

The matrix for the passage through a whole transfer line is then obtained by multiplication of the matrices of all the transfer line elements  $M = M_1 \cdot M_2 \cdot M_3 \dots$

A focusing/defocusing element is called a 'thin lens' if the *focal length*  $f = 1/(\kappa l)$  is much longer than the length of the element  $l$ . In this case one can approximate the transfer matrices by

$$M_F^* = \begin{pmatrix} 1 & 0 \\ -\frac{1}{f} & 1 \end{pmatrix} \quad (95)$$

$$M_D^* = \begin{pmatrix} 1 & 0 \\ \frac{1}{f} & 1 \end{pmatrix} \quad (96)$$

## 4.2 Periodic Focusing Channels

When  $\kappa(s)$  is a periodic function,

$$\kappa(s) = \kappa(s + L)$$

we are interested in a solution of (89) that has a form similar to that of a harmonic oscillator. The general solution is written

$$x(s) = \sqrt{\epsilon} w(s) \cos(\psi(s) + \psi_0) \quad (97)$$

where  $\epsilon$  and  $\psi_0$  are constants determined by the initial conditions. The *phase advance* per period or cell is

$$\sigma = \psi(s) - \psi(s + L) \quad (98)$$

The amplitude function  $w(s)$  is determined through the envelope equation:

$$w'' - \frac{1}{w^3} + \kappa(s)w = 0 \quad (99)$$

and

$$\psi' = \frac{1}{w^2} \quad (100)$$

Therefore the phase advance can be calculated from

$$\sigma = \int_s^{s+L} \frac{ds}{w^2}. \quad (101)$$

Introducing the so called Twiss parameters or betatron functions

$$\hat{\beta} = w^2(s), \quad \hat{\alpha} = -\frac{1}{2}\hat{\beta}', \quad \hat{\gamma} = \frac{1 + \hat{\alpha}^2}{\hat{\beta}} \quad (102)$$

one can show that at any point  $s$  along the accelerator all particles with the same initial  $\epsilon$ , but different  $\psi_0$  lie on the invariant trace space ellipse

$$\hat{\gamma}(s)x^2 + 2\hat{\alpha}(s)xx' + \hat{\beta}(s)x'^2 = \epsilon \quad (103)$$

The ellipse is illustrated in Fig. 20. For different locations through the lattice, the ellipses will have different shapes and orientation, but they will all have the same value of  $\epsilon$  (see Fig. 21).

We are looking for solutions where the ellipse, and so the Twiss parameters, at the entrance of a cell is the same as the ellipse at the exit. The



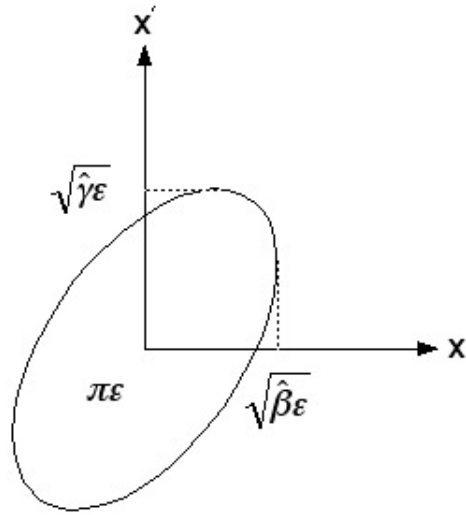


Figure 20: Trace-space ellipse.

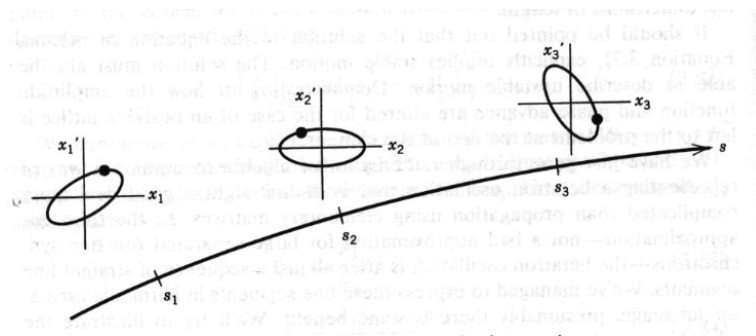


Figure 21: Phase space ellipses along the design trajectory.

Twiss parameters then have the same periodicity as the focusing function  $\kappa(s) = \kappa(s + L)$ . The transfer matrix in terms of the twiss parameters through one period can then be written (exercise !) as

$$\tilde{M} = \tilde{M}(s + L|s) = \begin{pmatrix} \cos \sigma + \hat{\alpha} \sin \sigma & \hat{\beta} \sin \sigma \\ -\hat{\gamma} \sin \sigma & \cos \sigma - \hat{\alpha} \sin \sigma \end{pmatrix} \quad (104)$$

with the phase advance per cell  $\sigma$  and the periodic Twiss parameters at the cell boundaries. For the phase advance we obtain

$$\cos \sigma = \frac{1}{2} \text{Tr} \tilde{M} \quad (105)$$

Stable betatron motion requires  $|\cos \sigma| < 1$  and so

$$-2 < \text{Tr} \tilde{M} < 2. \quad (106)$$

This criteria holds for periodic and non-periodic beam lines.

### 4.3 Emittance, Envelope and Admittance

The phase space area occupied by the beam is defined by the maximum value of  $\epsilon$ , or the largest ellipse, which we call emittance of the beam  $\epsilon_x$ . The *beam envelope* (see also Fig. 20) is characterized by the maximum value of  $x$

$$x_m(s) = \sqrt{\hat{\beta}(s)\epsilon_x} = w(s)\sqrt{\epsilon_x} \quad (107)$$

In a given accelerator or focusing channel the particle motion is usually restricted by the vacuum chamber or other structures. If  $x = a$  denotes the maximum excursion of the particle trajectory permitted by these aperture constraints, the *admittance* of the system in the  $x$ -direction is defined by  $\epsilon_{x,\max} = a^2/\hat{\beta}$ . Substitution of  $x_m$  into (99) yields the beam envelope equation

$$x_m'' - \frac{\epsilon_x^2}{x_m^3} + \kappa(s)x_m = 0 \quad (108)$$

In periodic focusing channels with  $\kappa(s) = \kappa(s + L)$  the *matched beam envelope* is defined as  $x_m(s) = x_m(s + L)$ . If the beam is not matched to the focusing channel there will be additional oscillations of the beam envelope. If the beam distribution  $f$  in the 4-dimensional trace space is a function of the emittances only, than it is a matched distribution

$$f(x, x', y, y') = f(\epsilon_x, \epsilon_y)$$

with the corresponding beam profile

$$\rho(x, y) = \int f(x, x', y, y') dx' dy'$$

and the rms beam radius

$$\sigma^2 = \widetilde{x^2} = \int x^2 \rho(x, y) dx dy$$

An example is a Gaussian beam distribution with the resulting profile

$$\rho(x, y) = A \exp\left(-\frac{x^2 + y^2}{2\sigma^2}\right)$$

for a symmetric beam. For a given beam distribution we define the rms emittance as

$$\tilde{\epsilon}_x = \sqrt{\widetilde{x^2 x'^2} - \widetilde{x x'}^2} \quad (109)$$

From this definition the rms beam envelope results as

$$\tilde{x}(s) = \sqrt{\hat{\beta}(s) \tilde{\epsilon}_x}$$

As an example Fig. 22 shows a measured beam profile in the GSI linear accelerator UNILAC at 4.7 MeV/u. The profile is measured using the fluorescence light from the residual gas (P. Forck et al., GSI Scientific Report 2003).

## 4.4 FODO Quadrupole Channel

Most beam transport lines, ring accelerators or storage rings consist of periodic sequences of focusing/defocusing quadrupole magnets. This concept is called 'strong focusing'. By contrast 'weak focusing' in circular accelerators is the principle that nearby circles, described by charged particles moving in a uniform magnetic field, only intersect once per revolution. Strong focusing was first invented at Brookhaven National Laboratory and deployed on the Alternating Gradient Synchrotron there. The theory (described partly in Sec. 4.2) was developed in 1957 by E. D. Courant and H. S. Snyder. Courant and Snyder found that the net effect of alternating the field gradient was that both the vertical and horizontal focusing of protons could be made strong at the same time, allowing tight control of proton paths in the machine. This increased beam intensity while reducing the overall construction cost of a more powerful accelerator.

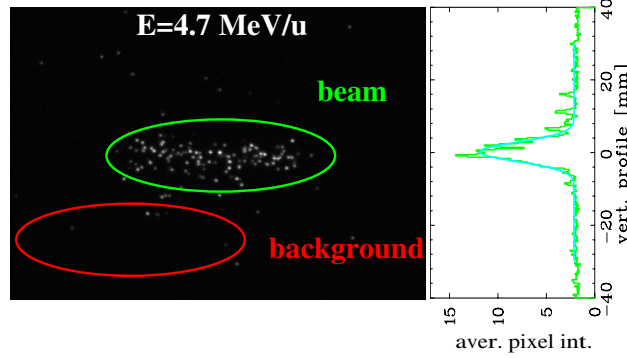


Figure 22: Image of a  $U^{28+}$  beam with  $I=0.7$  mA recorded during one UNILAC macro-pulse with a vacuum pressure of about  $10^{-5}$  mbar. The two dimensional image from the intensifier (left) and the projection for the vertical beam profile (right) is shown.

Here we want to discuss the properties of a 'FODO' focusing cell, where 'F' stands for a focusing quadrupole, 'D' for a defocusing quadrupole and 'O' for a drift section. We start with the thin lens approximation. Afterwards the more general representation in terms of finite length quadrupoles will be analyzed.

#### 4.4.1 Thin elements

Let  $L$  be the length of the FODO cell (see Fig. 23), then the transformation matrix for the cell is

$$\tilde{M} = M_F^* M_0 M_D^* M_0$$

$$\tilde{M} = \begin{pmatrix} 1 + \frac{L}{2f} & L + \frac{L^2}{4f} \\ -\frac{L}{2f^2} & 1 - \frac{L}{2f} - \frac{L^2}{4f^2} \end{pmatrix} \quad (110)$$

where  $M_F^*$ ,  $M_D^*$  are given by Eqs. 95, 96 and  $M_0$  is a drift with  $l = L/2$ . From the  $\tilde{M}$  we can obtain the phase advance per cell

$$\cos \sigma = \frac{1}{2} \text{Tr} \tilde{M} = 1 - \frac{L^2}{8f^2} \quad (111)$$

The equation allows one to compute the phase advance per cell from  $L$  and  $f$ . Stability requires  $|\cos \sigma| < 1$  or

$$f > \frac{L}{4} \quad (112)$$

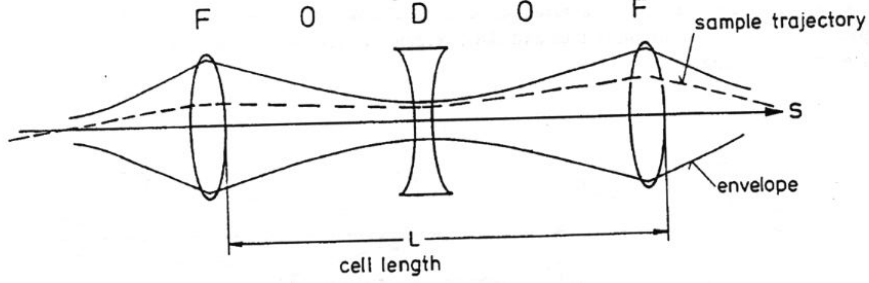


Figure 23: A thin lens FODO cell.

By comparing the matrix  $\tilde{M}$  in Eq. 110 with Eq. 104 we obtain for the Twiss parameter  $\hat{\beta}$  in the focusing quadrupole

$$\hat{\beta} = \frac{L + L^2/(4f)}{\sin \sigma} \quad (113)$$

#### 4.4.2 Thick elements

As an example for a general periodic focusing system we consider a finite length quadrupole channel in the FODO configuration. One period of such a channel is defined by a quadrupole of length  $l_Q$  that is focusing in  $x$  and defocusing in  $y$ , a quadrupole that is defocusing in  $x$  and focusing in  $y$  and two drift sections of length  $l_D$  each, as illustrated in Fig. 24. The force function  $\kappa(s)$ , which is piecewise constant, is indicated in the figure. The transfer matrix  $\tilde{M}$  for one period of such a FODO channel can be calculated by multiplication of the appropriate matrices.

$$\tilde{M} = \tilde{M}(s + L|s) = M_F M_O M_D M_O \quad (114)$$

Comparing (104) with the matrix (114) yields the phase advance per cell and the matched Twiss parameters at the boundaries. For the phase advance we obtain

$$\cos \sigma = \frac{1}{2} \text{Tr} \tilde{M}$$

or

$$\cos \sigma = \cos \theta \cosh \theta + \frac{l_D}{l_Q} \theta (\cos \theta \sinh \theta - \sin \theta \cosh \theta) - \frac{1}{2} \left( \frac{l_D}{l_Q} \right)^2 \theta^2 \sin \theta \sinh \theta$$

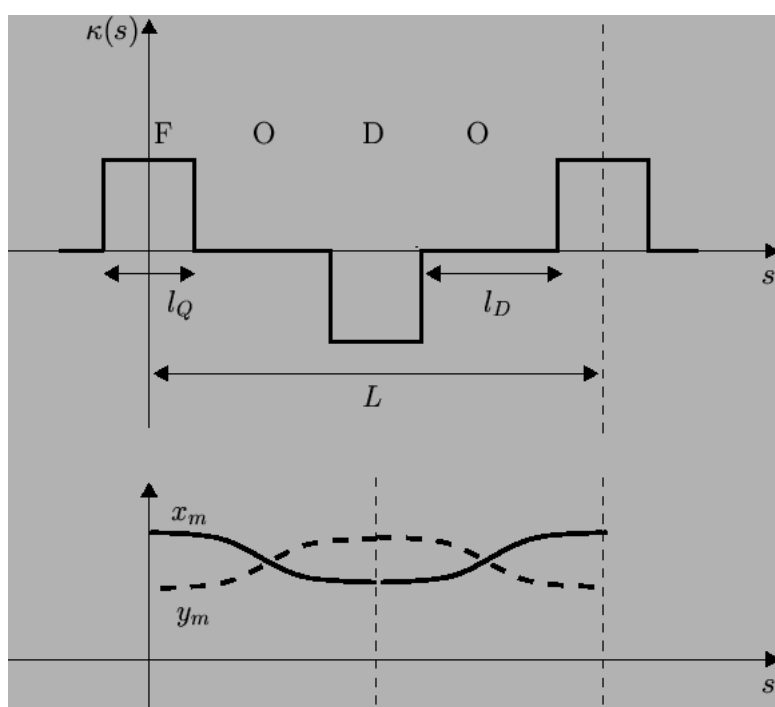


Figure 24: Force function  $\kappa(s)$  and matched envelopes  $x_m(s)$  and  $y_m(s)$  in a FODO channel.

with  $\theta = \sqrt{\kappa}l_Q$ . From the Twiss parameters at the entrance of the cell the parameters at arbitrary  $s$  can be calculated using the Twiss matrix

$$B = \begin{pmatrix} \hat{\beta} & -\hat{\alpha} \\ -\hat{\alpha} & \hat{\gamma} \end{pmatrix}$$

and their transformation law

$$B(s) = M(s) \cdot B_0 \cdot M^T(s)$$

The resulting matched functions  $\hat{\beta}_x(s)$  and  $\hat{\beta}_y(s)$  obtained with the lattice design computer program MAD-X<sup>†</sup> for  $l_D = 5$  m,  $l_Q = 4$  m and  $\sigma = 90^\circ$  are shown in Fig. 25. The MAD-X script describing all the input parameters is

```
TITLE,'Simple FODO without bends';

!----- DRIFT SPACES DEFINITION -----

dr: drift, L=5.0;

! ----- QUADRUPOLES -----

qf: quadrupole, L= 4.0, K1= 0.01;
qd: quadrupole, L= 4.0, K1= -0.01;

! ----- LINE DEFINITION -----

mycell: line=(qf,dr,qd,dr);

!-----

beam;
use, period=mycell;

!-----MATCHING-----

match,sequence=mycell;
VARY,NAME=qf->K1,STEP=0.0001;
VARY,NAME=qd->K1,STEP=0.0001;
```

---

<sup>†</sup><http://mad.home.cern.ch/mad/>

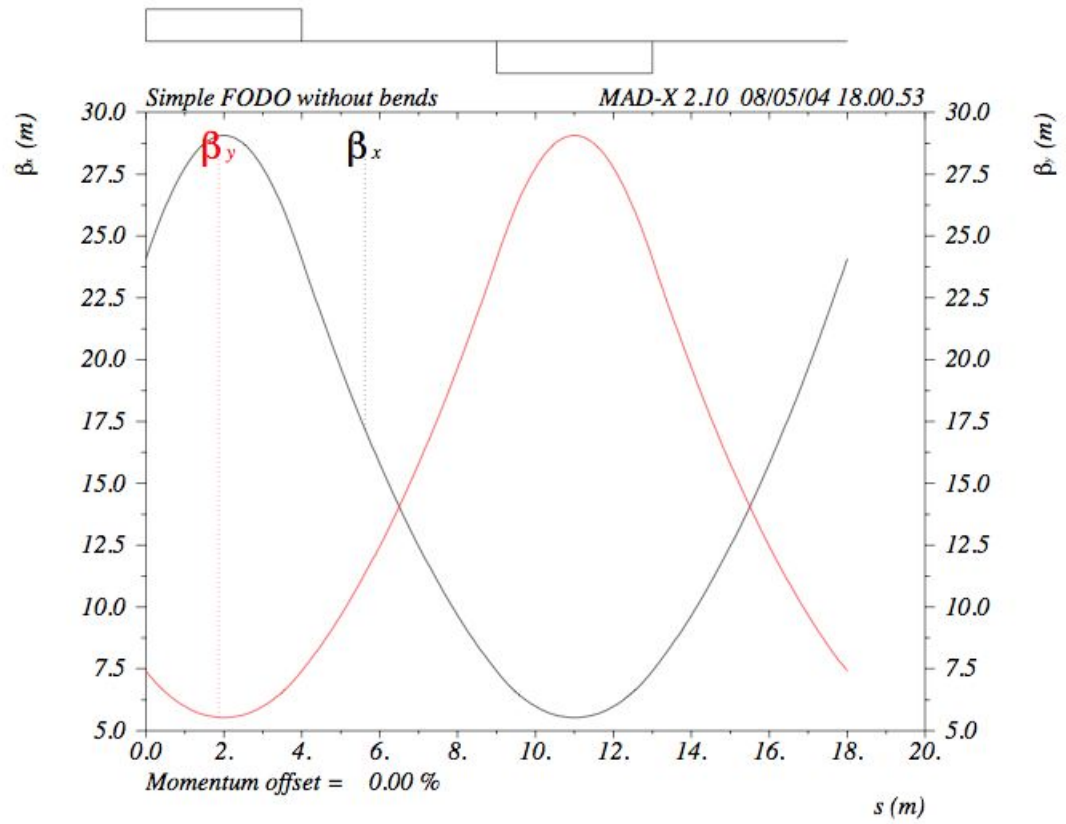


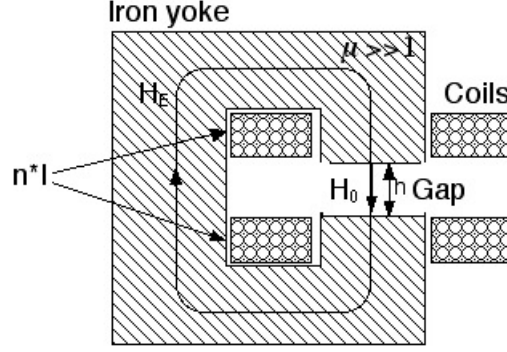
Figure 25: Lattice functions for a FODO focusing cell obtained with MAD.

```
CONSTRAINT,sequence=mycell,RANGE=#E,MUX=0.25,MUY=0.25;
LMDIF,CALLS=2000,TOLERANCE=1.0E-8;
endmatch;
```

```
!-----
```

```
setplot,post=2,ascale=1.5,lscale=1.5,rscale=1.5,sscale=1.5,lwidth=3;
PLOT, HAXIS=S,VAXIS1=BETX,VAXIS2=BETY,interpolate=true,colour=100;
```





$$nI = \oint \vec{H} d\vec{s} = H_E l_E + H_0 h \approx H_0 h \Rightarrow B = \mu_0 \frac{nI}{h}$$

Figure 26: Cross section and field calculation for a typical dipole accelerator magnet.

## 4.5 Dipole magnets and bending angle

The iron yoke and the field calculation for a dipole magnet are shown in Fig. 26. From the Lorentz force with a constant magnetic field  $B_y$  the bending radius results as  $R_0 = p_0/(qB_y)$ , with the momentum  $p_0$  of the ideal particle. The bending angle  $\theta$  in a dipole magnet of length  $l$  is (see Fig. 27)

$$\theta = \frac{q}{p_0} \int_{s_1}^{s_2} B_y ds \approx \frac{l}{R}.$$

The bending angle for the ideal particle in a dipole magnet of length  $l$  and field  $B_y$  is determined through (see also Fig. 27)

$$\theta = \frac{q}{p_0} \int_{s_1}^{s_2} B_y ds \approx \frac{q}{p_0} B_y l = \frac{l}{R_0}. \quad (115)$$

We now want to examine the transverse particle motion in a transport section that consists of dipole magnets and quadrupoles. Particles differing in momentum from that of the ideal particle (*off-momentum particles*) will be deflected in bending magnets by a different angle  $\Delta\theta = \theta(\Delta p/p)$  than the ideal particle (see Fig. 28).

This will have an important effect on the particle motion in curved transport lines or in circular accelerators. In order to examine the effects of different momenta more in detail we have to solve the resulting equation of motion in the horizontal plane

$$x'' + \kappa(s)x = \frac{1}{R(s)} \frac{\Delta p}{p_0} \quad (116)$$

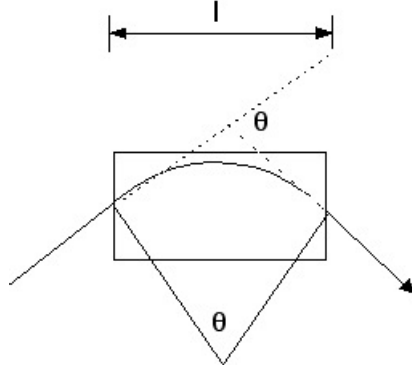


Figure 27: Bending of the particle trajectory in a dipole magnet.

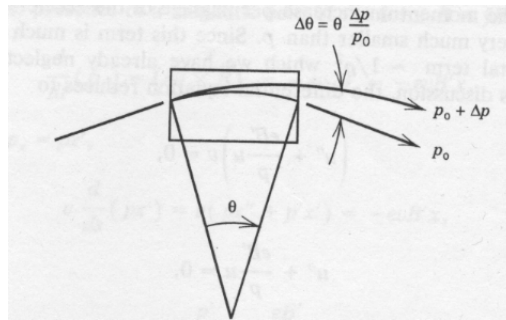


Figure 28: Bending of off-momentum particle trajectories in a dipole magnet.

the term on the rhs proportional to the momentum spread results directly from  $\Delta\theta = \theta(\Delta p/p_0)$ . This term is zero outside of the bending magnets ( $R \rightarrow \infty$ ).  $\kappa$  is assumed to be finite and constant only in quadrupole magnets and zero outside. Let us first search for a general solution for Eq. 116. The general solution  $x(s)$  is the sum of the complete solution  $x_\beta(s)$  of the homogenous equation and a particular solution  $x_D(s)$  of the inhomogenous equation

$$x(s) = x_\beta(s) + x_D(s) \quad (117)$$

An off-momentum particle performs betatron oscillation, described by  $x_\beta(s)$ , about a new closed orbit  $x_D(s)$ , that can be written as

$$x_D(s) = D(s) \frac{\Delta p}{p} \quad (118)$$

with the momentum dispersion function  $D(s)$  (see also Fig. 29). The dispersion function is a solution of

$$D'' + \kappa D = \frac{1}{R} \quad (119)$$

which can be interpreted as the equation of motion for a particle with  $\Delta p/p = 1$ . In circular accelerators we look for solution with  $D(s+C) = D(s)$ , where  $C$  is the ring circumference. Like in the treatment of betatron oscillations we use a "piecewise" method, assuming constant  $\kappa$  and  $R$  inside focusing or bending elements. We can again adapt the matrix approach used in Sec. 4.1 for betatron oscillations. The general solution can be written as

$$\begin{pmatrix} D \\ D' \end{pmatrix}_1 = \begin{pmatrix} a & b \\ c & d \end{pmatrix} \begin{pmatrix} D \\ D' \end{pmatrix}_0 + \begin{pmatrix} e \\ f \end{pmatrix}$$

where the two-by-two matrix is the same as for the treatment of betatron oscillations. For  $\kappa > 0$  we obtain  $e = (1 - \cos(\sqrt{\kappa}l))/(R\kappa)$  and  $f = \sin(\sqrt{\kappa}l)/(R\sqrt{\kappa})$ . For  $\kappa = 0$  we get  $e = l^2/(2R)$  and  $f = l/R$ . By the addition of a third trivial equation,  $1 = 1$ , the equation above can be expressed in terms of a three-by-three matrix

$$\begin{pmatrix} D \\ D' \\ 1 \end{pmatrix} = M_B \begin{pmatrix} D_0 \\ D'_0 \\ 1 \end{pmatrix}$$

with

$$M_B = \begin{pmatrix} a & b & e \\ c & d & f \\ 0 & 0 & 1 \end{pmatrix} \quad (120)$$

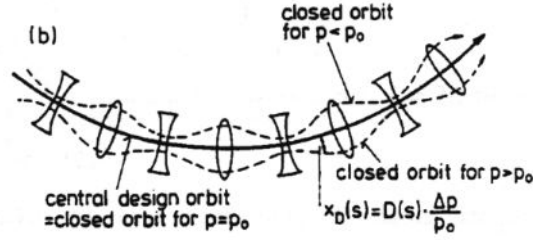


Figure 29: Closed orbit for particles with momentum  $p \neq p_0$  in a circular accelerator with FODO cells.

Note that the same  $3 \times 3$  matrices propagate either the dispersion function or the trajectory itself. That is  $M_B$  operates on the vector

$$\begin{pmatrix} D \\ D' \\ 1 \end{pmatrix}$$

or on the vector

$$\begin{pmatrix} x \\ x' \\ \frac{\Delta p}{p} \end{pmatrix}$$

The same procedure can be carried out starting at any point in the lattice, and so the dispersion function can be computed everywhere. In simple situations, the dispersion function will be everywhere positive; that is, orbits of higher momenta than the design orbit are at larger radius.

## 5 Synchrotrons

A synchrotron is a particular type of cyclic particle accelerator in which the magnetic field (to bend the particles) and the electric field (to accelerate the particles) are carefully synchronized with the circulating particle beam (see Fig. 30). The first electron synchrotron was constructed 1945 by Edwin McMillan in the USA. While a cyclotron uses a constant magnetic field and a constant-frequency applied electric field, both of these fields are varied in the synchrotron. By increasing these parameters as the particles gain energy, their path can be held constant as they are accelerated.

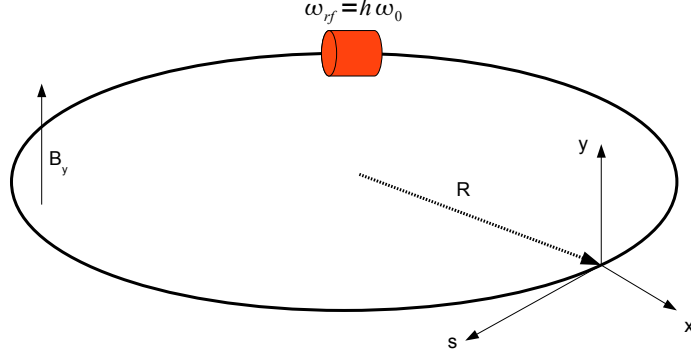


Figure 30: Synchrotron of radius  $R$ , with rf cavity, bending field  $B_y$  and the local coordinate system following the ideal particle.

This allows the magnet aperture to be small. A synchrotron usually consists of bending magnets (dipoles), focusing magnets (quadrupoles) and straight drift sections. The straight sections are required for the rf cavities and for other ring components, like injection and extraction systems. The beam is injected into the synchrotron from a pre-accelerator, that can be a linac or a smaller synchrotron. The maximum energy that a cyclic accelerator can impart is typically limited by the strength of the magnetic field(s) and the radius of the particle path. Figs. 31 and 32 show the GSI synchrotron SIS (SchwerIonenSynchrotron).

Dipole magnets are used to guide the beam along the circular orbit. The total bending angle for a circular accelerator is  $2\pi$ , and the total integrated dipole field is

$$\oint B_y ds = 2\pi p_s / q = 2\pi B_0 R_0$$

$B_0 R_0 = p_0 / q$  is called the momentum rigidity of the beam. Here  $R_0$  is the bending radius. The revolution frequency of the ideal particle is

$$\omega_0 = \frac{v_0}{R} = \frac{q B_y}{\gamma_0 m} \quad (121)$$

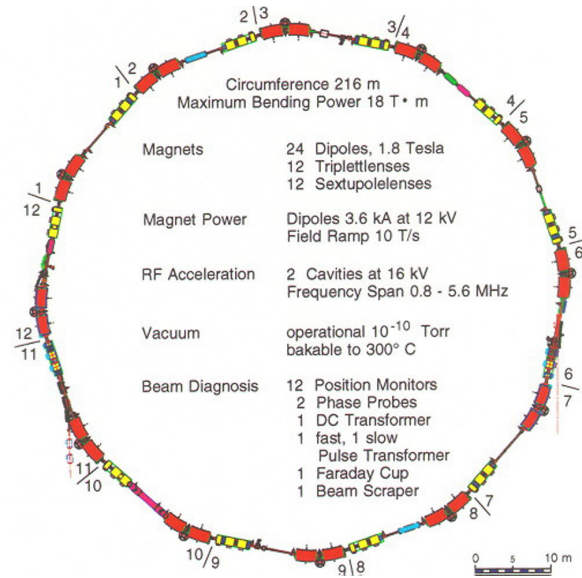


Figure 31: The GSI synchrotron SIS-18.

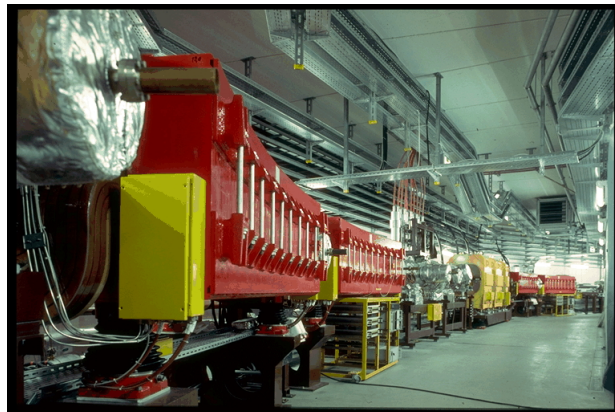


Figure 32: View in the SIS tunnel with quadrupole and dipole magnets.

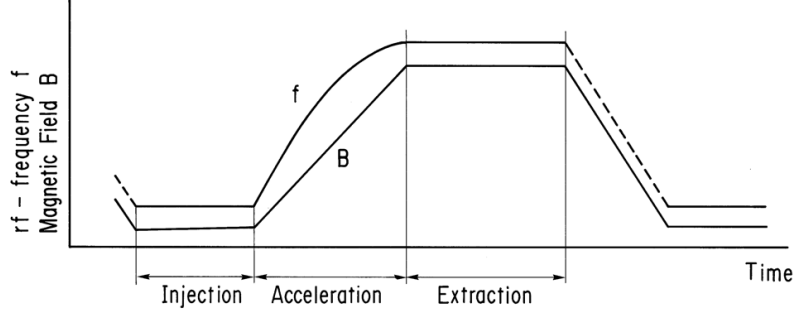


Figure 33: A typical synchrotron cycle. Shown are example ramps for the magnets and the rf frequency.

with the actual radius  $R$  of the synchrotron.

Transverse focusing is provided in a synchrotron through quadrupole magnets that are usually grouped in focusing cells of length  $L$ . In case of a circular accelerators with circumference  $C = NL$  one uses in place of the betatron phase advance  $\sigma$  (see Eq. 98) the machine tune

$$Q = \nu = \frac{N\sigma}{2\pi} \quad (122)$$

which is the number of *betatron oscillations* in one revolution, also known as *betatron tune*.

## 5.1 Acceleration in a synchrotron

During acceleration the magnetic field  $B_y$  is ramped synchronously with the rf frequency (see Fig. 33). The rf frequency is related to the magnetic bending field  $B_y$  via

$$f_{rf} = hf_0 = \frac{c^2 h q B_y}{2\pi W_0} \quad (123)$$

where  $f_0$  is the revolution frequency,  $h$  the harmonic number and  $W_0 = \gamma_0 mc^2$  the particle energy. If the particles approach the speed of light the relation turns into

$$f_{rf} \rightarrow h \frac{c}{2\pi R}. \quad (124)$$

Next we want to calculate a criteria for the rf voltage amplitude  $V_0$ . The energy of the ideal particle is

$$W_0 = \sqrt{(p_0 c)^2 + (mc^2)^2} \quad (125)$$

from the above relation one obtains

$$\Delta W_0 = v_0 \Delta p_0 \quad (126)$$

for the dependence of the energy change on the momentum change during acceleration. The momentum change can be obtained from the rigidity  $p_0 = qB_y R_0$  as

$$\Delta p_0 = q R_0 \Delta B_y \quad (127)$$

By eliminating  $\Delta p_0$  we arrive at

$$\Delta W_0 = 2\pi q R_0 R \frac{\Delta B_y}{T_0} \quad (128)$$

where  $T_0 = 2\pi R/v_0$  is the revolution period. The energy gain per turn for the ideal particle is

$$\Delta W_0 = q V_0 \cos \phi_s \quad (129)$$

and one obtains

$$R_0 \dot{B}_y = \frac{V_0}{2\pi R} \cos \phi_s \quad (130)$$

for the relation between the magnet ramping rate and the rf voltage per circumference. For a fixed ramping rate and voltage amplitude we can determine  $\phi_s$  from the above relation. With increasing ramping rate also  $\phi_s$  increases. Therefore the bucket area shrinks. In order to accelerator a bunch with a given bunch area a sufficiently large voltage amplitude has to be chosen.

## 5.2 Momentum compaction factor

In a synchrotron the difference in path length between off-momentum orbits and the design orbit is characterized by the *compaction factor*  $\alpha$ , which is defined as

$$\frac{\Delta C}{C} = \alpha \frac{\Delta p}{p} \quad (131)$$

where  $C$  is the accelerator circumference. The circumference change  $\Delta C$  is given by

$$\Delta C = \oint \left( R + D \frac{\Delta p}{p} \right) d\theta - \oint R d\theta \quad (132)$$

with the dispersion function  $D(s)$ . For the fractional circumference change we therefore have

$$\frac{\Delta C}{C} = \frac{\Delta p}{p} \frac{1}{C} \oint \frac{D}{R} ds \quad (133)$$



or

$$\alpha = \frac{1}{\gamma_t^2} = \left\langle \frac{D}{R} \right\rangle \quad (134)$$

with the transition energy  $\gamma_t$ .

### 5.3 Steering and Focusing Errors

Thus far we have described an accelerator where each magnetic or electric element performs exactly its pre-described task. In particular, for a circular accelerator, there is by design an ideal reference orbit which closes on itself and about which betatron oscillation would occur for particles with nonzero emittance. Suppose that a particular bending magnet has a field somewhat different from its intended value. We will show, that the field imperfection leads to a new closed orbit near, but different from, the ideal design orbit.

Suppose that in our otherwise ideal circular accelerator a single steering error of magnitude  $\Delta x' = \theta$  (with  $\theta = l\Delta B/(BR)$ ) is located at  $s = 0$ , where  $\Delta B$  is an unintentional uniform dipole field over the path length  $l$ . Because of this small steering error  $x = 0$  is no longer a solution of the equation of motion. Everywhere except at the location of the steering error, however, the equation of motion is still that of a betatron oscillation. Only at the point of the error is the equation inhomogeneous.

Let the orbit immediately downstream of the deflection  $\theta$  be specified by  $x_0, x'_0$ . To propagate this initial condition around the ring, we just multiply by the single turn matrix  $M$  (Eq. 104 with  $\sigma = 2\pi Q$ ). Now we are immediately upstream of the deflection. To close the orbit we need only to add the angle  $\theta$  and demand that we be back to  $x_0, x'_0$ . In symbols,

$$M \begin{pmatrix} x_0 \\ x'_0 \end{pmatrix} + \begin{pmatrix} 0 \\ \theta \end{pmatrix} = \begin{pmatrix} x_0 \\ x'_0 \end{pmatrix} \quad (135)$$

Solving for  $x_0$  and  $x'_0$ ,

$$\begin{pmatrix} x_0 \\ x'_0 \end{pmatrix} = (I - M)^{-1} \begin{pmatrix} 0 \\ \theta \end{pmatrix} \quad (136)$$

with the identity matrix  $I$ . Inserting  $M$  from Eq. 104, with the Twiss parameters taken at  $x_0, x'_0$ , after some algebra (exercise !) we arrive at the following expression for the closed orbit at  $s = 0$

$$\begin{pmatrix} x_0 \\ x'_0 \end{pmatrix} = (I - M)^{-1} \begin{pmatrix} 0 \\ \theta \end{pmatrix} = \frac{\theta}{2 \sin \pi Q} \begin{pmatrix} \hat{\beta}_0 \cos \pi Q \\ \sin \pi Q - \hat{\alpha}_0 \cos \pi Q \end{pmatrix} \quad (137)$$

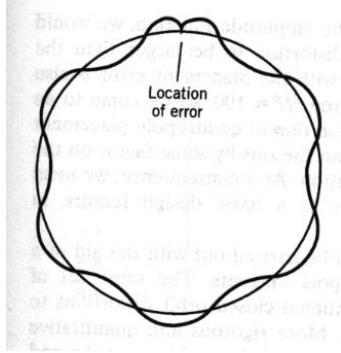


Figure 34: Sketch of the close orbit in presence of a single steering error.

The closed orbit may now be expressed as a function of position around the ring, by applying the transfer matrix between one point and another. The solution for the closed orbit is sketched in Fig. 34. We see that the new closed orbit in the presence of a single steering error exhibits a cusp at the location of the error. Particles whose initial conditions do not coincide with this closed orbit will perform betatron oscillations around the new closed orbit.

In reality there will be as many steering errors as there are magnetic elements in the accelerator. As a consequence every large circular accelerator needs a set of independently powered steering dipole magnets in order to correct closed orbit distortions.

From Eq. 137 we observe that there is no closed orbit if the tune  $Q$  is an integer. This is the most elementary example of a resonance driven by lattice errors. If the tune were an integer the steering errors would just reinforce from turn to turn until the oscillation amplitude is large enough to strike the wall of the vacuum chamber.

We will now briefly discuss the effects of focusing or gradient errors. Let there be a single gradient error  $\Delta\kappa$  of length  $ds$  equivalent to a thin quadrupole with the focal length length  $f = 1/(\Delta\kappa ds)$

$$M_F^* = \begin{pmatrix} 1 & 0 \\ -\frac{1}{f} & 1 \end{pmatrix} \quad (138)$$

The matrix for a single turn is then  $M = M_0 M_F^*$ , where  $M_0$  is the matrix for the ideal ring. From the trace of  $M$  it follows that

$$\cos 2\pi Q = \cos 2\pi Q_0 - \frac{1}{2} \frac{\hat{\beta}_0}{f} \sin 2\pi Q_0 \quad (139)$$

where  $Q$  and  $Q_0$  are the new and old tunes respectively, and  $\hat{\beta}_0$  is the original amplitude function at the point of the perturbation. Assuming that the perturbation is small, we can obtain a useful expression for the *tune shift* due to a gradient error by writing

$$Q = Q_0 + \Delta Q \quad (140)$$

and expanding the cosine term on the left hand side of the last equation. The result is

$$\Delta Q = \frac{1}{4\pi} \frac{\hat{\beta}_0}{f} \quad (141)$$

If there is a distribution of gradient errors, this last result generalizes to

$$\Delta Q = \frac{1}{4\pi} \oint \hat{\beta}(s) \Delta \kappa(s) ds \quad (142)$$

where we used  $1/f = \Delta \kappa ds$ . We see that the effect of gradient errors is a tune shift. If the tune is near a integer or half integer the  $Q$  value obtained from Eq. 139 becomes complex. There will be a range of values of  $Q_0$  for which the motion is unstable; this range is called *stopband*. Here we just quote the general result for error driven resonances, including also nonlinear error fields and horizontal-vertical coupling effects

$$nQ_x + mQ_y = p \quad (143)$$

where  $n$ ,  $m$  and  $p$  are integers.  $|n| + |m|$  is the order of the resonance driving error (dipole 1, quadrupole 2, sextupole 3, ...). An gradient error causes second order resonances. Because of manufacturing errors and the finite length of the magnetic components all orders of error field are usually present in a ring accelerator. The strength of the errors fields drops with increasing order. The working point  $(Q_x, Q_y)$  must be sufficiently far away from dangerous low order resonances. Fig. 35 shows the resonance lines up to third order together with a possible working point.

### 5.3.1 Chromaticity

In Sec. 4.5 we discussed the motion of off-momentum particles in bending magnets. Also the focusing strength (Eq. 88) depends on momentum

$$\kappa = \kappa_0 + \Delta \kappa \quad (144)$$

with

$$\Delta \kappa = -\frac{\Delta p}{p} \kappa_0$$

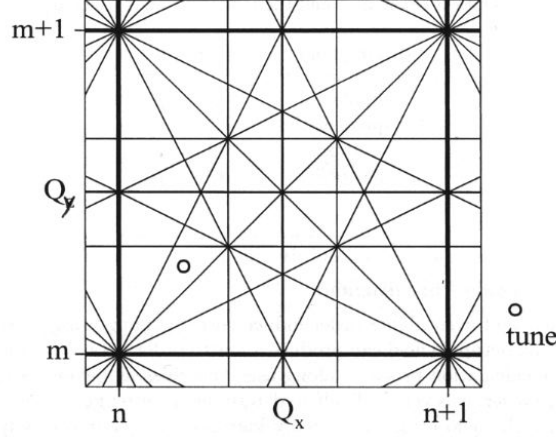


Figure 35: Resonances up to 3rd order in both planes of oscillation. A possible working point is indicated.

for small momentum spread. This momentum dependency can be interpreted as a focusing error for off-momentum particles. Using Eq. 142 the corresponding tune shift can be calculated as

$$\xi = \frac{\Delta Q}{\Delta p/p} = -\frac{1}{4\pi} \oint \hat{\beta}(s) \kappa_0(s) ds \quad (145)$$

with the *chromaticity*  $\xi$ . Why worry about chromaticity ? There are two reasons. If the beam has a large momentum spread, then a large chromaticity may place some portion of the beam on resonances. Secondly there are intensity dependent instabilities connected to a finite chromaticity. The capabilities for chromaticity adjustment provided by the linear lattice are limited. What is needed is a magnet that represents a gradient that is a function of momentum. A distribution of sextupole magnets located at locations with finite dispersion is usually used for this purpose. The field of a sextupole magnet (see Fig. 36) is of the form (with the constant  $g$ )

$$B_x = gxy \quad (146)$$

$$B_y = \frac{1}{2}g(x^2 - y^2)$$

The corresponding gradients are

$$\frac{\partial B_y}{\partial x} = gx \quad (147)$$

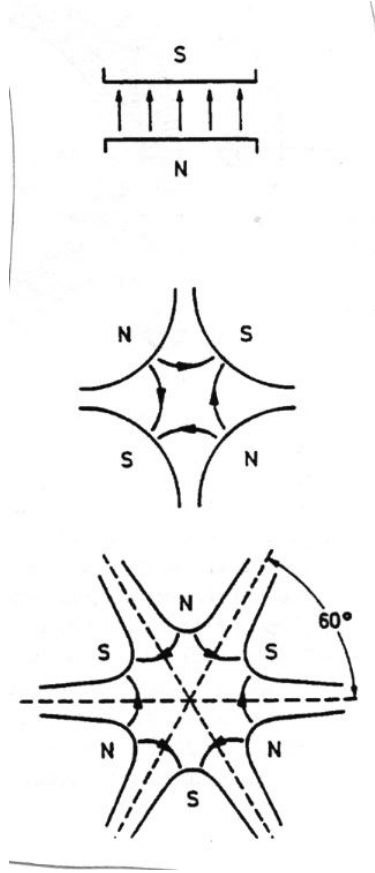


Figure 36: Yoke profiles for dipole, quadrupole and sextupole magnets.

$$\frac{\partial B_x}{\partial y} = gx$$

the focusing strength is therefore

$$\kappa_{sext} = \frac{q}{p}gx = mx \quad (148)$$

The resulting field gradient at a location with finite dispersion function is

$$\kappa_{sext} = mD \frac{\Delta p}{p}$$

and the contribution to the chromaticity from sextupoles may be readily calculated.

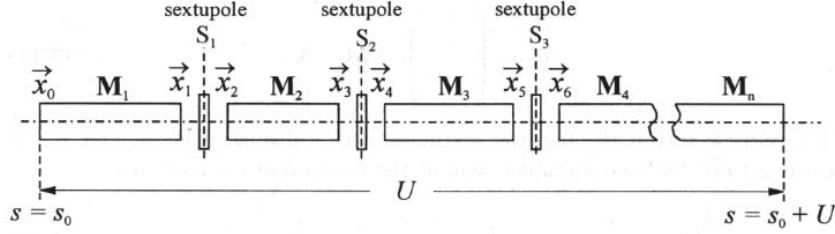


Figure 37: Magnet structure with thin sextupoles.

## 5.4 Restriction of dynamic aperture by sextupoles

The sextupole magnets needed to compensate for the chromaticity unfortunately also have negative effects on the dynamic behaviour of the beam. This is due to the fact that the quadratic field distribution adds a non-linear force on the particles, leading to anharmonic betatron oscillations. Non-linear resonances may thus arise, leading to sudden particles loss above a certain betatron amplitude (*'dynamic aperture'*). One faces the phenomenon of *chaotic particle dynamics*. It is not possible to treat this non-linear problem analytically, and one is forced to use numerical methods instead. Here we consider a simple magnet structure with a thin sextupole after each linear focusing cell (Fig. 37). The linear focusing sections are again described by their transfer matrix  $M$  (e.g. Eq. 104). The sextupoles may then be approximated by thin lenses with no longitudinal extend. If  $l$  is the length of the  $n$ th sextupole then the change in trajectory angle induced by the sextupole field (Eq. 146) in both planes is given through (using  $x'' = -qB_y/p$  and  $y'' = qB_x/p$ )

$$\Delta x' = -\frac{q}{p}B_y l = -\frac{1}{2}(ml)(x_n^2 - y_n^2) \quad (149)$$

$$\Delta y' = \frac{q}{p}B_x l = (ml)x_n y_n$$

with the displacements  $x_n, y_n$  at the  $n$ th sextupole. We consider the motion of a particle with zero betatron amplitude in vertical direction ( $y(s) = 0$ ), then the horizontal coordinates of the particle right behind the  $n$ th thin sextupole are

$$\vec{x}_n = \begin{pmatrix} x_n \\ x'_n + \Delta x' \end{pmatrix} \quad (150)$$

with  $\Delta x' = -1/2(ml)x_n^2$ . The evolution of the trajectory through the

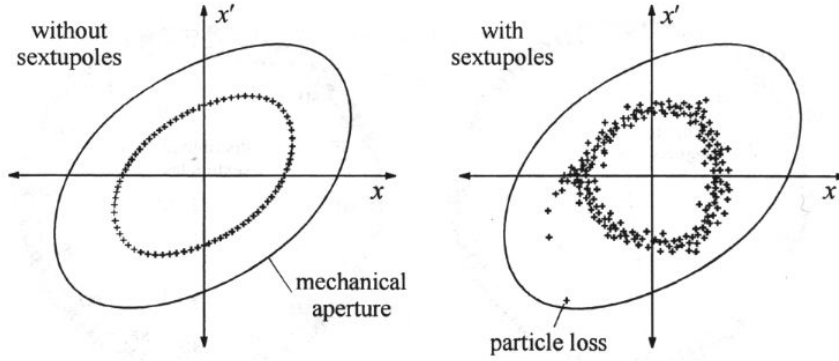


Figure 38: Particle tracking through a circular accelerator (left without sextupole, right with sextupoles).

sextupole cannot be described by the usual matrix formalism because the matrix elements would then themselves depend on the starting values of the vector. Therefore the change in angle induced by the sextupole must be explicitly added to the trajectory vector. The evolution of the particle coordinates through the focusing structure including the sextupole is then given through

$$\begin{pmatrix} x_{n+1} \\ x'_{n+1} \end{pmatrix} = M \begin{pmatrix} x_n \\ x'_n - 1/2(ml)x_n^2 \end{pmatrix} \quad (151)$$

This equation must be iterated for a range of initial conditions and for sufficiently many cells. This procedure is called *particle tracking*. The result of such a computation is shown in Fig. 38. From this example we see that sextupoles reduce the stable region in phase space. Stable particle motion is only possible for small betatron oscillation amplitudes. If the amplitude exceeds a certain value, which may be much smaller than the physical acceptance given by the size of the vacuum chamber, then the particle is lost. The reduced area is called dynamical aperture. Extensive numerical particle tracking studies are required to obtain the optimum sextupole positions and strengths for maximum dynamic aperture.

## 5.5 Vacuum pipes and eddy currents

One important component of a synchrotron is the vacuum pipe. It encloses the vacuum of  $10^{-9}$  mbar (proton machines) up to  $10^{-12}$  mbar (heavy-ions or 'cold' machines). Usually the pipe is made of stainless steel. The pipe must

be able to shield the EM fields generated by the circulating beam. Therefore a good conductor must be chosen for the pipe material. However, we will see in the following that the ramping  $B_y$  creates eddy currents in the conducting beam pipe. A sketch of a dipole magnet with a rectangular vacuum chamber is shown in Fig. 39. The height of the pipe is  $h$  and its width  $2b$ . According to Faraday's law the time dependent  $B_y$  creates an electric field along the loop characterized by the positions  $\pm x$  from the chamber center

$$\oint \vec{E} \cdot d\vec{l} = - \int \dot{\vec{B}} \cdot d\vec{S} \quad (152)$$

and

$$E_z = \dot{B}_y x \quad (153)$$

For finite conductivity the current density is

$$j_z = \sigma E_z = \sigma \dot{B}_y x \quad (154)$$

The total current within the area between  $x = 0$  and  $x$  is

$$I = d\sigma \dot{B}_y x^2 \quad (155)$$

where  $d$  is the thickness of the chamber and the contribution from the top and bottom have been included. From Ampere's law we obtain the magnetic field difference

$$\Delta B_y = \mu_0 \frac{d}{h} \sigma \dot{B}_y (x^2 - b^2) \quad (156)$$

which is a dipole and a sextupole field. The sextupole field induced by the eddy currents usually represent a significant field perturbation. In addition the eddy currents will heat the beam pipe. The power loss per unit length can be obtained from Ohm's law

$$dP = d\sigma^{-1} j_z^2(x) l dx \quad (157)$$

and

$$\frac{P}{l} = d\sigma b^3 \dot{B}^2 \quad (158)$$

The heating of the wall causes the outgassing of molecules, which increases the vacuum pressure. From the above expressions for the sextupole field and for the power loss we can see that both effects are proportional to the the conductivity  $\sigma$  and the thickness of the chamber  $d$ . In fast ramping synchrotrons (up to 5 Hz) one choses a thin (0.3 mm), stainless steel beam pipe in the dipole sections in order to reduce eddy currents effects and still enable a sufficient shielding of the EM fields generated by the beam. In rapid cycling synchrotrons ceramic pipes with wire cages or with out rf shields (copper stripes) are employed.



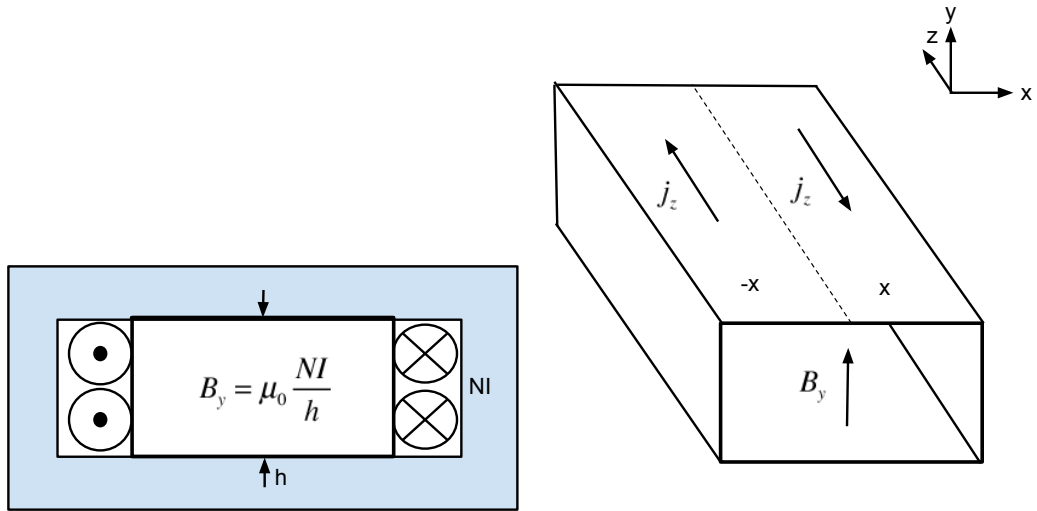


Figure 39: Dipole magnet with rectangular vacuum pipe.

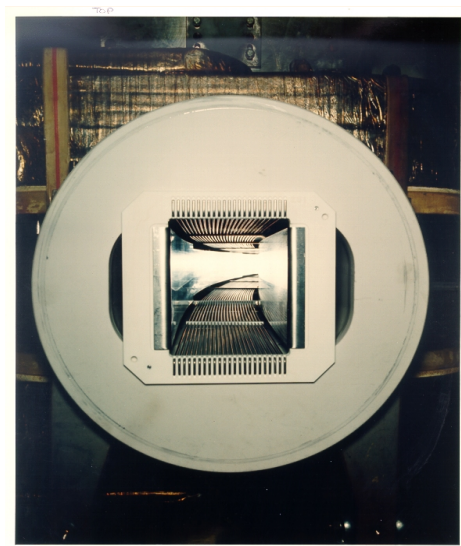


Figure 40: Ceramic vacuum chamber with wire cage of the ISIS rapid cycling synchrotron (RAL, UK).

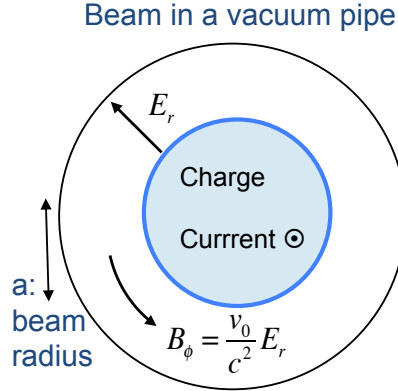


Figure 41: Vacuum chamber and beam envelope.

## 6 Beam intensity effects

Thus far, we have considered only the motion of a single particle, or of a beam of noninteracting particles, in the presence of external forces. Many of the important phenomena in accelerator physics involve the interplay between the beam and its surroundings through the electromagnetic fields induced by the beam. First the transverse space charge force and its effect on the betatron oscillation tunes will be introduced. Afterwards longitudinal effects will be considered.

### 6.1 Transverse intensity effects

#### 6.1.1 Transverse space charge

Consider the simple example of uniform cylindrical beam. Within our simple model the beam has a circular cross section with radius  $a = a_x = a_y$  and propagates through a ideal conducting beam pipe (Fig. 41). It is assumed that the variation of the beam size with distance  $s$  is slow enough that the axial electric field and the radial magnetic field can be neglected. If the uniform charge density of the beam is ( $r^2 = x^2 + y^2$ )

$$\rho(r, s) = \begin{cases} \rho_0(s) & : r \leq a \\ 0 & : r > a \end{cases}$$

with

$$\rho_0(s) = \frac{I}{\pi v_0 a^2(s)}$$

From the application of Gauss's law we obtain for the radial electric field

$$E(r) = \begin{cases} \frac{Ir}{2\pi\epsilon_0 a^2 v_0} & : r \leq a \\ \frac{I}{2\pi\epsilon_0 v_0 r} & : r > a \end{cases} \quad (159)$$

from Ampere's law, with the current density  $j = \rho v_0$ , the magnetic field is obtained as

$$B(r) = \begin{cases} \frac{\mu_0 I r}{2\pi a^2} & : r \leq a \\ \frac{\mu_0 I}{2\pi r} & : r > a \end{cases} \quad (160)$$

The resulting space charge force on an individual beam particle located at  $r < a$  inside the beam profile is

$$F = q(E - v_0 B) = q(1 - \beta_0^2)E = \frac{qE}{\gamma_0^2} \quad (161)$$

with the relativistic parameters  $\beta = v_0/c$  and  $\gamma_0$ . Thus the attractive magnetic force, which becomes significant at high velocities, tends to compensate for the repulsive electric force. Therefore, space charge defocusing is primarily a nonrelativistic effect. In accelerators, however, beams are carried from low to high energies and therefore space charge effects may become important during some or all phase of acceleration. This is specifically true for protons and heavy ions for which the relativistic  $\gamma_0$  is rather low for most achievable particle energies. It is worth to notice that electric or magnetic space charge field at relativistic energies can still be important due the presence of the metallic beam pipe or due to a partial compensation of the beam's charge density (self-focusing).

For non-round beam profiles with  $a_x \neq a_y$  we obtain the space charge force (exercise)

$$F_x = q(1 - \beta_0^2)E = \frac{qE_x}{\gamma_0^2} = \frac{Ix}{\pi\epsilon_0 v_0} \frac{1}{a_x(a_x + a_y)} \quad (162)$$

### 6.1.2 Equation of Motion with Space Charge

The space charge force can be added to the linear equation of motion (Eq. 89) in the following way

$$x'' + \kappa_x(s)x = \frac{1}{\gamma m v_0^2} \times (\text{space charge force}) \quad (163)$$

Here we will neglect the effect of bending magnets. Using the space charge force for a uniform, non-round beam we have

$$x'' + \left( \kappa_x(s) - \frac{2K}{a_x(s)(a_x(s) + a_y(s))} \right) x = 0 \quad (164)$$

with the *perveance*

$$K = \frac{qI}{2\pi\epsilon_0 mc^3 \beta^3 \gamma^3} \quad (165)$$

The space charge force acts as a distributed defocusing error in the equation of motion. The beam envelopes  $a_x$  and  $a_y$  can be obtained from the envelope equations including the space charge force

$$a_x'' + \kappa_x(s)a_x - \frac{2K}{a_x(s) + a_y(s)} - \frac{\epsilon_x^2}{a_x^3(s)} = 0 \quad (166)$$

The equation for  $a_y$  can be obtained by simply replacing  $x$  and  $y$ . The envelope equation can be solved analytically in the limit of a constant focusing gradient  $\kappa_x$  and a corresponding zero-current phase advance  $\mu_0 = \sqrt{\kappa_x}L$ , where  $L$  is the cell length. If we furthermore assume  $\kappa_x = \kappa_y = \kappa_0$  we arrive at

$$\kappa_0 a - \frac{K}{a} - \frac{\epsilon^2}{a^3} = 0 \quad (167)$$

where  $a = a_x = a_y$  is the beam envelope. Introducing the space charge modified focusing gradient

$$\kappa = \kappa_0 - \frac{K}{a} \quad (168)$$

we obtain

$$\kappa a - \frac{\epsilon^2}{a^3} = 0 \quad (169)$$

or

$$\sqrt{\kappa} a^2 = \epsilon \quad (170)$$

In terms of the phase advance the above expression can be expressed as

$$\left( \frac{\mu}{L} \right)^2 = \left( \frac{\mu_0}{L} \right)^2 - \frac{K}{a} \quad (171)$$

The general solution for the beam envelope can be obtained from Eq. 167 as

$$a = a_0 \left( u + \sqrt{1 + u^2} \right)^{1/2} \quad (172)$$

where  $u$  is the dimensionless parameter

$$u = \frac{K}{2\sqrt{\kappa_0}\epsilon} \quad (173)$$

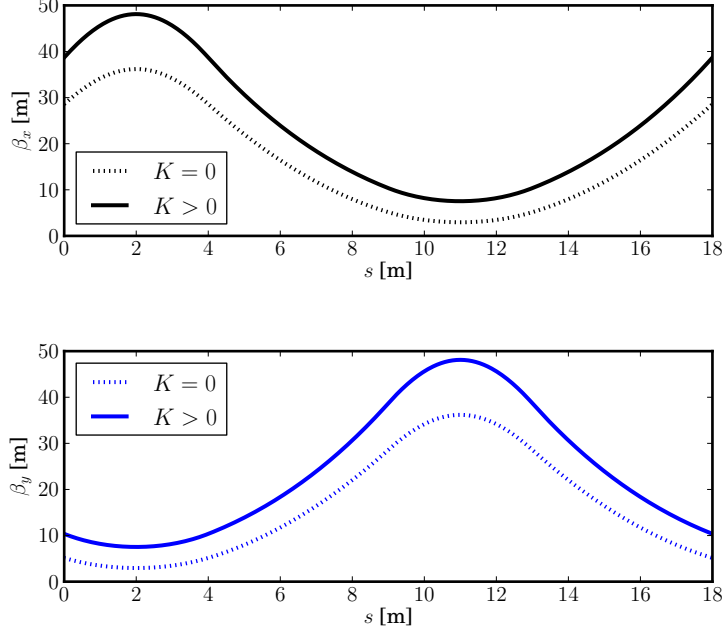


Figure 42:  $\hat{\beta}$  functions in a FODO cell with and without space charge.

and  $a_0$  is the beam envelope for zero-current ( $K = 0$  and  $u = 0$ )

$$\sqrt{\kappa_0} a_0^2 = \epsilon \quad (174)$$

For  $u \gg 1$  we can neglect the contribution of the emittance to the beam envelope in Eq. 167 and  $a$  is determined by the balance of the external focusing force and the defocusing space charge force

$$a = \sqrt{\frac{K}{\kappa_0}} \quad (175)$$

In the general case of non-constant focusing gradients  $\kappa_x(s)$  the envelope equations Eq. 166 have to be solved numerically in order to obtain the stationary envelopes  $a_x(s)$  and  $a_y(s)$ . The corresponding  $\hat{\beta}$ -functions are given through  $\hat{\beta}_x = a_x^2/\epsilon_x$ . The  $\hat{\beta}$ -functions obtained numerically for a space charge induced phase shift reduction  $\Delta\mu = \mu - \mu_0 = 60^\circ$  are shown in Fig. 42.

### 6.1.3 Space Charge Tune Shift

Here we will take a closer look to the (usually weak) space charge tune shift in a circular accelerator. The effect of space charge is equivalent to a distributed gradient error

$$\Delta\kappa(s) = -\frac{2K}{a_x(a_x + a_y)} \quad (176)$$

The resulting tune shift can be calculated from Eq. 142

$$\Delta Q = -\frac{1}{4\pi} \oint \hat{\beta}(s) \frac{2K}{a_x(a_x + a_y)} ds \quad (177)$$

Using the definition of the beam envelope  $a_x = \sqrt{\hat{\beta}\epsilon_x}$  we obtain

$$\Delta Q = -\frac{1}{4\pi} \oint \frac{2K}{\epsilon_x(1 + a_y/a_x)} ds \approx -\frac{KR}{\epsilon_x \left(1 + \sqrt{\epsilon_y/\epsilon_x}\right)} \quad (178)$$

We see that the tune is decreased due to the defocusing character of the transverse space charge force. As a figure of merit one often considers a maximum tolerable space charge tune shift of  $|\Delta Q| < 0.25$  in order to avoid crossing of low order error resonances in circular machines. For a coasting (dc) beam with a homogenous transverse charge distribution  $\rho = \text{const.}$  it would be sufficient to adjust the tune in order to avoid resonances. However, for a transverse Gaussian charge distribution the tune depends on the oscillation amplitude, as we will see in the next section. If the beam is bunched the space tune shift reaches its maximum at the bunch center and falls to zero at the bunch ends. Therefore the tune shift is a tune spread, that cannot be compensated by the external, linear focusing forces.

### 6.1.4 Nonlinear space charge force

The homogenous charge density used in the preceding sections simplifies considerably the analytic estimation of space charge effects. A more realistic model is a Gaussian charge distribution given through

$$\rho(r) = \frac{I}{2\pi\beta_0 c \sigma^2} \exp\left(-\frac{r^2}{2\sigma^2}\right) \quad (179)$$

with the beam current

$$I = 2\pi\beta_0 c \int_0^\infty \rho(r) r dr \quad (180)$$

and with rms beam radius  $\sigma$ . For a homogenous beam profile  $\rho = \text{const.}$  we obtain the rms radius  $\sigma = r_m/2$ . The transverse electric field for a Gaussian charge distribution results as

$$E(r) = \frac{I}{2\pi\epsilon_0 v_0 r} \left[ 1 - \exp\left(-\frac{r^2}{2\sigma^2}\right) \right] \quad (181)$$

and the force is

$$F(r) = \frac{qE(r)}{\gamma^2} \approx \frac{qI}{2\pi\epsilon_0\gamma_0^2 v_0} \frac{r}{2\sigma^2} \quad (182)$$

The force is no longer linear. Only for  $r \ll \sigma$  the force can be linearized. The resulting approximate expression is given on the rhs of the above equation. The force close to the center of a Gaussian beam profile is twice as large as the force resulting from a homogenous profile. In the case of the Gaussian profile the space charge force drops for larger  $r$ , resulting in a *tune spread*.

### 6.1.5 Beam-beam tune shift

In a collider ring two beams circulating in opposite directions are brought into collisions. Suppose one bunch collides head-on with a another bunch moving in the opposite direction. Let the bunches both have the cross-sectional area  $A$  and the particle number  $N_b$ . Any particle in one bunch will see a fraction of the area of the other bunch  $N\sigma_c/A$ , where  $\sigma_c$  is the cross-section for the interaction of two particles. The interactions per passage of two bunches is then  $N_b^2\sigma_c/A$ . If the frequency of bunch collisions is  $f$ , then the interaction rate is  $fN_b^2\sigma_c/A$ . The *luminosity* is defined as the interaction rate per unit cross section

$$L = f \frac{N_b^2}{A} \quad (183)$$

The luminosity represents a figure of merit for a collider. Suppose the beams have a round, homogenous density profile. The area would then simply be  $A = \pi a^2$ , where  $a = x_m = y_m$ . Luminosities are often expressed in cgs units. For instance the CERN LHC presently operates at luminosities of the order  $10^{33} \text{ cm}^{-2} \text{ s}^{-1}$ .

At the interaction point the two bunches feel the electric and magnetic forces of the other bunch. In the following we will assume that both bunches travel at the speed of light ( $v_0 = c$ ). The force exerted by the beam moving in one direction exerted on a 'test particle' in the other beam is (see also Eq. 161)

$$F = q(E + cB) = 2qE = \frac{q^2\lambda r}{\pi\epsilon_0 a^2} \quad (184)$$

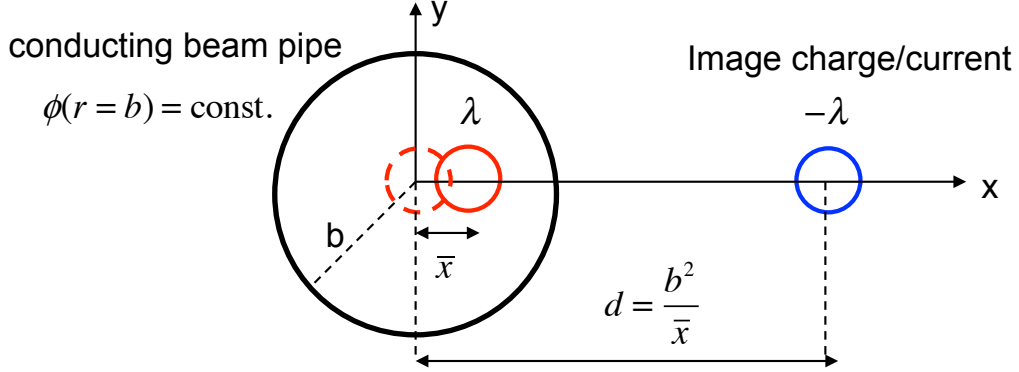


Figure 43: A beam with a horizontal offset in a cylindrical beam pipe. The image fields can be obtained from an image beam at a distance  $h = b^2/\bar{x}$  from the actual beam.

where  $\lambda(s)$  is the line density of the beam moving in the opposite direction. The magnetic field is now defocusing because of the opposite direction of the velocity. We can now calculate the induced gradient error as

$$\Delta\kappa(s) = -\frac{q^2\lambda(s)}{\pi\epsilon_0 m\gamma_0 a^2} \quad (185)$$

and the beam-beam tune shift per collision

$$\begin{aligned} \Delta Q &= \frac{1}{4\pi} \oint \frac{a^2}{\epsilon_x} \Delta\kappa(s) ds = \frac{1}{2} \times \frac{1}{4\pi\epsilon_x} \int a^2 \Delta\kappa(s) ds \\ &= -\frac{q^2 N_b}{8\pi^2 \epsilon_0 m\gamma_0 \epsilon_x} \end{aligned} \quad (186)$$

During a collision the force is felt only during the time that the two bunches are colliding. Only half of the integral over the bunch length is necessary, because the two bunches are traveling in opposite directions. The tolerable beam-beam tune shift is usually smaller than the tolerable space charge tune shift, because the beam in a collider is stored for hours, whereas the space charge tune shift is effective at injection energy, where the beam remains usually only for ms.

### 6.1.6 Image fields and transverse impedances

In this section we will derive the transverse image force and the corresponding impedance on a beam with a horizontal offset  $\bar{x}$  in a beam pipe (see Fig. 43).



The image electric and magnetic field acting on the beam center can be obtained from an image charge and current at  $h = b^2/\bar{x}$ , where  $b$  is the pipe radius.

$$E_x = \frac{q\lambda}{2\pi\epsilon_0 h} \quad (187)$$

$$B_y = \frac{\mu_0 I}{2\pi h} \quad (188)$$

The electric image force on the beam center is

$$F_x = \frac{qE_x}{\gamma_0^2} = \frac{q^2\lambda\bar{x}}{2\pi\epsilon_0\gamma_0^2 b^2} \quad (189)$$

The surface charge density can be obtained from

$$\rho_s = \epsilon_0 E_r(r = b) \quad (190)$$

and results as

$$\rho_s(\phi) \approx \frac{q\lambda\bar{x}}{\pi b^2} \cos \phi \quad (191)$$

For the total charge on the pipe wall one obtains

$$\lambda_s = \int_{-\pi/2}^{\pi/2} \rho_s(\phi) b d\phi = \frac{2}{\pi} \frac{\lambda\bar{x}}{b} \quad (192)$$

The electric field can be obtained from the surface charge density as

$$E_x = \frac{1}{2\pi\epsilon_0} \int_0^{2\pi} \rho_s(\phi) \cos \phi d\phi \quad (193)$$

In a similar fashion one can obtain the surface current density

$$j_s(\phi) = \frac{I\bar{x}}{\pi b^2} \cos \phi \quad (194)$$

and the total current in the pipe wall

$$I_s = \int_{-\pi/2}^{\pi/2} j_s(\phi) b d\phi = \frac{2}{\pi} \frac{I\bar{x}}{b} \quad (195)$$

The transverse impedance is defined as the force divided by the beam's dipole moment

$$Z_x(\omega) = \frac{-i}{\beta_0 I\bar{x}} \left( E_x + \left[ \vec{v}_0 \times \vec{B} \right]_x \right) \quad (196)$$

Using the above expression for the electric and magnetic image forces we obtain the transverse impedance for a ideally conducting pipe as

$$Z_x = -i \frac{Z_0}{2\pi(\beta_0\gamma_0)^2 b^2} \quad (197)$$

where the vacuum impedance is

$$Z_0 = (\varepsilon_0 c)^{-1} = 377 \, \Omega \quad (198)$$

In the following we will account for a finite surface conductivity  $\sigma_s = \sigma_w d$  of the pipe wall (wall thickness  $d$ , bulk wall conductivity  $\sigma_w$ ). Then the longitudinal electric field due to the surface current density  $j_s$  in the wall is

$$E_z = \frac{j_s}{\sigma_s} \quad (199)$$

If we assume a beam offset oscillation frequency  $\omega$

$$\bar{x}(t) = \hat{x} \exp(-i\omega t) \quad (200)$$

where  $\hat{x}$  is the oscillation amplitude, then the induced magnetic field in the pipe is

$$B_y = \hat{B}_y \exp(-i\omega t) \quad (201)$$

and (see Fig. 44)

$$\hat{B}_y = -i \frac{\hat{E}_z}{\omega b} = i \frac{\hat{j}_s}{b d \sigma_w \omega} \quad (202)$$

This dipole magnetic field can be used in Eq. 197 and one obtains the transverse impedance due to the finite conductivity of the pipe wall as

$$Z_x(\omega) = \frac{c}{\pi b^3 d \sigma_w \omega}, \quad d \ll \delta_w \quad (203)$$

where

$$\delta_w = \sqrt{\frac{2}{\mu_0 \sigma_w \omega}} \quad (204)$$

is the skin depth. The above expression for the transverse resistive wall impedance assumes a constant wall current ( $d \ll \delta_w$ ) and low frequencies. For higher frequencies the thickness  $d$  should be replaced by the skin depth  $\delta_w$ .

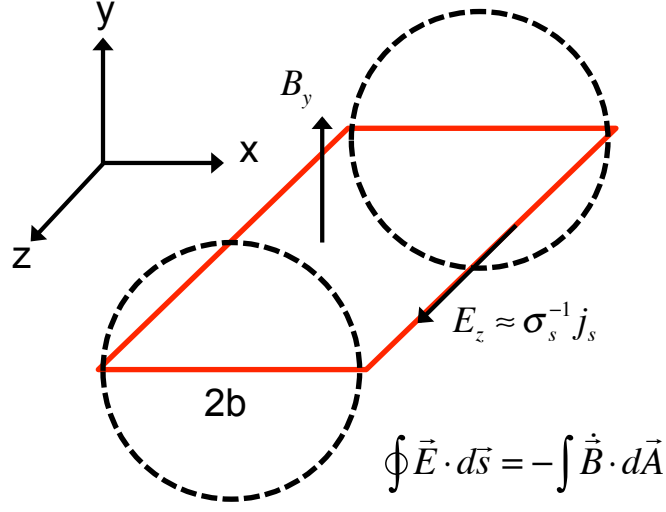


Figure 44: Integration path (red lines) for the induced magnetic field.

### 6.1.7 Transverse coherent beam oscillations

The transverse offset for a given beam density  $\rho(x, y, s)$  is

$$\bar{x}(s) = \int x \rho(x, y, s) dx dy \quad (205)$$

The equation of motion for the beam offset is obtained from the single particle equation of motion and the definition of the transverse impedance as

$$\bar{x}'' + \kappa_x \bar{x} = \frac{\bar{F}_x}{\gamma_0 m v_0^2} = i \frac{q I Z_x}{\beta_0 E_0} \bar{x} \quad (206)$$

The term on the lhs causes a shift of the coherent tune, meaning the betatron oscillation frequency of the center of the beam. The coherent tune shift is

$$\Delta Q_x^{coh} = \frac{1}{4\pi} \oint \hat{\beta}_x \Delta \kappa_x ds \approx -i \frac{q I R^2 Z_x}{2 Q \beta_0 E_0} \quad (207)$$

where  $\hat{\beta}_x \approx R/Q$  has been used. The imaginary part of the transverse wall impedance Eq.?? results in a real coherent tune shift

$$\text{Re}(\Delta Q_x^{coh}) = -\frac{q I R^2 Z_0}{2 Q_0 \beta_0^3 \gamma_0^2 b^2 E_0} \quad (208)$$

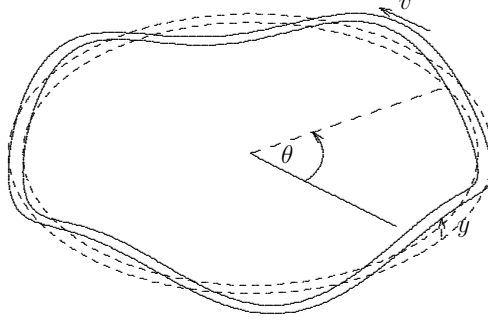


Figure 45: Coherent oscillations of a coasting beam in a synchrotron.

The real part Eq. 203 causes an imaginary tune shift and a corresponding exponential growth of the offset oscillation with the growth rate

$$\tau^{-1} = \omega_0 \text{Im}(\Delta Q_x^{coh}) = \omega_0 \frac{qIR^2c}{2\pi Q\beta_0 E_0 b^3 d\sigma_w \omega} \quad (209)$$

The growth rate depends on the frequency  $\omega$  of the offset oscillations seen by a stationary observer. Moving with the beam velocity the offset oscillations are given through

$$\bar{x}(t) = \hat{x} \exp(Q\omega_0(t - t_0)) \quad (210)$$

where  $t_0$  is A stationary observer at position  $s$  sees the offset (Fig. 45)

$$\bar{x}(s, t) = \hat{x} \exp(ns/L - \omega t) \quad (211)$$

where  $n$  is the harmonic number and  $L$  the circumference. If we set  $s = v_0 t$  and then compare the two expression we arrive at the coherent oscillation frequencies

$$\omega_n = (Q \pm n)\omega_0 \quad (212)$$

If we differentiate  $\omega_n$  with respect to the momentum deviation we arrive at

$$\Delta\omega_n = (\xi - \eta_0(n \pm Q))\omega_0 \frac{\Delta p}{p} \quad (213)$$

which results in a spread of the coherent frequency  $\Delta\omega_n$  for a beam with a momentum spread. The frequency spread causes a decay of the offset oscillations with the rate

$$\tau_n^{-1} \approx \delta\omega_n \quad (214)$$

For

$$\delta\omega_n \gtrsim \omega_0 \text{Im}\Delta Q_x^{coh} \quad (215)$$

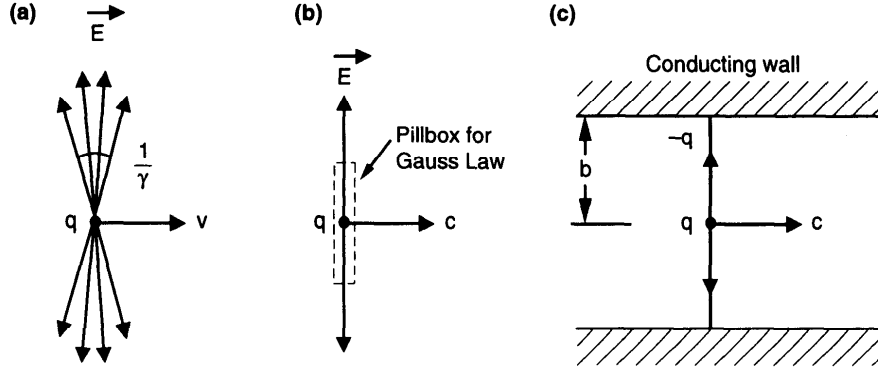


Figure 46: Electric field lines for a relativistic charge as seen in the laboratory system. a) free space, b) in a perfectly conducting pipe.

the offset oscillations are stabilized. This results in the stability criterion for the momentum spread

$$\frac{\Delta p}{p} > \frac{\omega_0}{(\eta_0 - (n - Q_0))} \frac{q I R^2 Z_x^R}{2 Q_0 \beta_0 E_0} \quad (216)$$

## 6.2 Longitudinal intensity effects

### 6.2.1 Field of a relativistic point charge

For relativistic energies the field distribution of a point charge is contracted into a thin disk with an angular spread on the order of  $1/\gamma$  (see Figure 46). An expression for the electric field can be obtained from the Lorentz transformation of the fields from the rest frame into the laboratory frame<sup>‡</sup>. The result for the electric field in cylindrical coordinates  $(r, z)$  is

$$\vec{E} = \frac{q \vec{r}}{4\pi\epsilon_0\gamma^2 (z^2 + r^2/\gamma^2)^{3/2}} \quad (217)$$

For an ultrarelativistic charge the magnitude of the electric field is easily obtained by drawing a pillbox with radius  $r$  and an infinitesimal height around the charge  $q$  (see Figure 46, b)) and then applying Gauss's law. The result is

$$E_r = \frac{q\lambda(s - ct)}{2\pi\epsilon_0 r} \quad (218)$$

<sup>‡</sup>J. D. Jackson, Classical electrodynamics

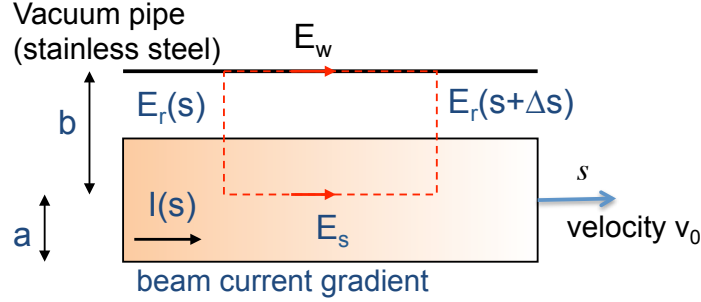


Figure 47: Uniformly distributed continuous beam of radius  $a$  in a beam pipe of radius  $b$ . The induced electric fields are shown schematically. The rectangular loop is used for the path integral of Faraday's law.

Similar, Ampere's law gives

$$B_\phi = \frac{q\mu_0\lambda(s - ct)}{2\pi r} \quad (219)$$

From the above equations one sees that the longitudinal fields are very weak at relativistic energies in case of an ideally conducting, smooth pipe. In the following we will analysis the longitudinal field for non-relativistic energies and also for resistive pipe walls.

### 6.2.2 Longitudinal space charge

Let  $a$  be the radius of a uniformly distributed continuous beam, and let  $b$  be the radius of the beam pipe. Then the transverse electromagnetic fields of the beam are determined through Eqs. 159 and 160.

Using Faraday's law

$$\oint \vec{E} \cdot d\vec{l} = -\frac{\partial}{\partial t} \int \vec{B} \cdot d\vec{A} \quad (220)$$

along the loop shown in Figure 47 we obtain

$$(E_s - E_w)\Delta s + \frac{qg}{4\pi\epsilon_0}(\lambda(s + \Delta s) - \lambda(s)) = -\Delta s \frac{g\mu_0}{4\pi} \frac{\partial I}{\partial t} \quad (221)$$

with the line charge density  $I = qv_0\lambda$ . The geometry factor  $g = 1 + 2\ln(b/a)$  is obtained from the integral along the radial paths from the beam center to the vacuum chamber wall. The electric field acting on the beam becomes

$$E_s = E_w - \frac{qg}{4\pi\epsilon_0} \left( \frac{\partial \lambda}{\partial s} + \frac{1}{c^2} \frac{\partial I}{\partial t} \right)$$

From the continuity equation  $\partial I / \partial t = -q(\beta c)^2 (\partial \lambda / \partial s)$  we obtain

$$E_s = E_w - \frac{qg}{4\pi\epsilon_0\gamma^2} \frac{\partial \lambda}{\partial s} \quad (222)$$

Ignoring the wall electric field (ideal conductor) we thus have

$$E_s = -\frac{qg}{4\pi\epsilon_0\gamma^2} \frac{\partial \lambda}{\partial s} \quad (223)$$

This electric field corresponds to an effective space charge voltage around the ring seen by a beam particle (ring radius  $R$ )

$$V_s = 2\pi R E_s \quad (224)$$

If we assume a coasting beam with a current modulation at the harmonic number  $n = \omega/\omega_0$  then the current signal observed at a fixed position  $\theta = s/R$  in a synchrotron is

$$I(s, t) = I_0 + I_n \exp(in\theta - i\omega t) \quad (225)$$

where  $I_n$  is the modulation amplitude. The corresponding longitudinal electric field is

$$E(s, t) = E_n \exp(in\theta - i\omega t) \quad (226)$$

and the longitudinal impedances is defined as

$$Z_s(\omega) = -\frac{V_n}{I_n} \quad (227)$$

where  $V_n = 2\pi R E_n$ . For an ideally conducting pipe we obtain from Eq. 223

$$Z_s = -\frac{ing}{2\epsilon_0\beta_0 c\gamma^2} \quad (228)$$

which is also called longitudinal space charge impedance. For a resistive pipe wall the longitudinal electric field in the wall is

$$E_w = \sigma_w^{-1} j_w \quad (229)$$

where  $j_w = I_w/(2\pi bd)$  is the current density in the wall. Again the wall current is assumed to be constant ( $d \ll \delta_w$ ) and furthermore it is assumed that the total wall current exactly compensates the beam current  $I \approx -I_w$ . The resulting real resistive wall impedance at low frequencies ( $d \ll \delta_w$ ) is

$$Z_s = \frac{R}{\sigma_w db} \quad (230)$$

For a resistive beam pipe the total impedance is given by the above real component plus the imaginary space charge impedance. We will see later that the real resistive wall impedance can cause longitudinal beam instabilities. The imaginary space charge impedance cause instabilities only above transition energy (negative mass instability). First we will analyze the effect of space charge on synchrotron oscillations.

### 6.2.3 Synchrotron oscillations with space charge

Here we will consider longitudinal motion in a stationary rf bucket ( $\phi_s = 0$ ) in a circular accelerator. Instead of the coordinate  $\phi$  we will use the distance from the synchronous particle  $z = h\Delta\phi/R$ . The longitudinal equation of motion can then be written as

$$z'' = \frac{qV(z)}{Cm^*v_0^2} \quad (231)$$

where  $V(z)$  is the voltage per turn,  $m^* = -\eta m/\gamma$  is the effective mass and  $C = 2\pi R$  the ring circumference. For the rf voltage  $V_{rf}(z) = -V_0 \sin(hz/R)$  and under the assumption of small amplitude synchrotron oscillations  $V_{rf}(z) \approx -V_0 hz/R$  we obtain

$$z'' = -\frac{\omega_s^2}{v_0^2} z \quad (232)$$

where  $\omega_s$  is the synchrotron frequency

$$\omega_s = \sqrt{\frac{2\pi h q V_0}{C^2 |m^*|}} \quad (233)$$

Let us assume a parabolic bunch profile (see also Fig. 48) given through

$$\lambda(z) = \frac{3}{4} \frac{N}{z_m} \left( 1 - \frac{z^2}{z_m^2} \right) \quad (234)$$

with the number of particles in the bunch  $N_b$  and the bunch half-width  $z_m$

$$N_b = \int_{-z_m}^{z_m} \lambda(z) dz \quad (235)$$

From Eq. 223 the longitudinal space charge field is obtained as

$$E_s(z) = \frac{3gqN_b}{2\varepsilon_0\gamma_0^2 z_m^3} z \quad (236)$$



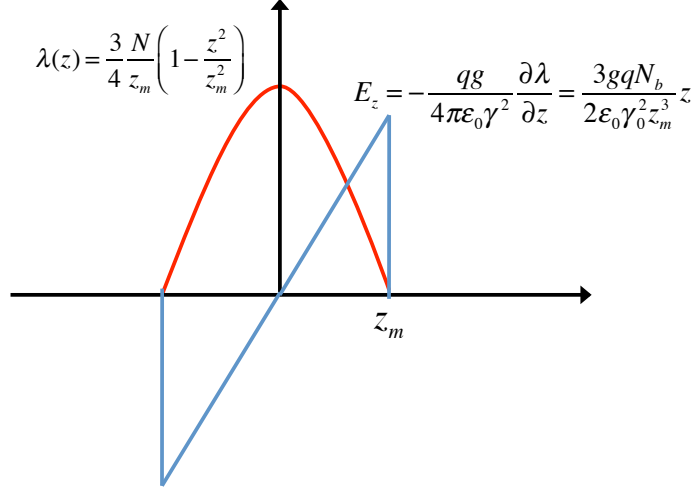


Figure 48: Parabolic bunch profile and the resulting space charge field.

and the space charge voltage per turn as  $V_s = E_s C$ . The total voltage seen by a beam particle is given by the sum of the rf voltage  $V_{rf}$  and the space charge voltage  $V_s$ . For a parabolic bunch space charge results in a linear force on the particles and we can write the equation of motion as

$$z'' = -\frac{\omega_s^2}{v_0^2} \left( 1 - \frac{K_L}{\omega_s^2 z_m^3} \right) z \quad (237)$$

with the longitudinal perveance

$$K_L = \frac{3\pi h g q^2 N_b}{2\epsilon_0 \gamma^2 C^2 m^*} \quad (238)$$

or in terms of the space charge impedance

$$K_L = \frac{3\pi q^2 v_0 N_b}{C^2} \left| \frac{Z_{sc}}{n} \right| \quad (239)$$

We see that the effective synchrotron frequency can be either reduced (defocusing, for  $m^* > 0$ , below transition) or increased (focusing, for  $m^* < 0$ , above transition). As a consequence, above transition, local density bumps can growth with time, leading to *self-bunching* of the beam. This effect is called the negative mass instability that will be treated in the next section.

#### 6.2.4 Space charge waves and instabilities

Modulations of the current profile can seed an instability that poses a serious problem for both high-current linear accelerators and circular machines.

This longitudinal instability affects the longitudinal particle distribution and limits the beam intensity. To understand the physical mechanism driving this instability it will first be useful to discuss how perturbations of the longitudinal charge density propagate along the beam as *space charge waves*. We start from the Vlasov equation for the longitudinal distribution function  $f(z, v_z, t)$

$$\frac{\partial f}{\partial t} + v_z \frac{\partial f}{\partial z} + \frac{qE_z}{m^*} \frac{\partial f}{\partial v_z} = 0$$

with the effective mass  $m^* = -\gamma m/\eta$ . The longitudinal electric field is obtained from

$$E_z = -\frac{g}{4\pi\epsilon_0\gamma^2} \frac{\partial \rho_L}{\partial z} = -\frac{X^{sc}}{2\pi} \frac{\partial I}{\partial z}$$

with the space charge reactance  $X^{sc}$  defined through

$$Z^{sc} = -inX^{sc}$$

and the current profile and line charge density

$$I(z, t) = \beta c \rho_L(z, t) = q\beta c \int_{-\infty}^{\infty} f(z, v_z, t) dv_z$$

In the *cold-beam approximation* we assume the distribution function

$$f(z, v_z, t) = \frac{1}{q\beta c} I(z, t) \delta(v_z - u(z, t))$$

and the Vlasov equation reduces to the cold-fluid equations for the local velocity  $u(z, t)$  and the line charge density  $\rho_L(z, t)$

$$\frac{\partial I}{\partial t} + \frac{\partial}{\partial z}(Iu) = 0$$

and

$$\frac{\partial u}{\partial t} + u \frac{\partial u}{\partial z} = -\frac{qX^{sc}}{2\pi m^*} \frac{\partial I}{\partial z}$$

Let us assume a beam with unperturbed dc current  $I_0$ , which implies that the longitudinal dc electric field is zero. To analyze the propagation of waves on a coasting (unbunched) beam we use the linearized, cold-fluid model for the small perturbations  $I_1$  and  $u_1$ , with

$$I = I_0 + I_1, \quad u = u_0 + u_1 = u_1$$

The linearized cold-fluid equations are

$$\frac{\partial I_1}{\partial t} + I_0 \frac{\partial u_1}{\partial z} = 0$$

and

$$\frac{\partial u_1}{\partial t} = -\frac{qX^{sc}}{2\pi m^*} \frac{\partial I_1}{\partial z}$$

In a circular machine (radius  $R$ ) the solutions can be written in the form of running waves

$$u_1 = u_n \exp(i\Delta\omega t - inz/R)$$

and

$$I_1 = I_n \exp(i\Delta\omega t - inz/R)$$

with the modulation amplitudes  $u_n$  and  $I_n$ , the harmonic number  $n$  and the *coherent frequency shift*  $\Delta\omega_n = \omega - n\omega_0$ . For  $m^* > 0$  the resulting constant phase velocity  $c_s$  is

$$c_s = \frac{R\Delta\omega}{n} = \pm \sqrt{\frac{qI_0 X^{sc}}{2\pi m^*}} \quad (240)$$

The backwards running wave ( $c_s > 0$ ) is called *slow space charge wave* and the forward running wave ( $c_s < 0$ ) is called *fast space charge wave*. Because of their similarity with ion sound waves in plasmas  $c_s$  is also called *speed of sound*.

As can be seen from the above results, for  $m^* > 0$  density perturbations in a coasting beam surrounded by a perfectly conducting drift-tube wall travel along the beam as fast and slow space charge waves. The frequency ( $\omega = \omega_n + \Delta\omega_n$ ) of the two waves are real, hence there is no change (growth or decay) of the wave amplitudes. The beam neither loses nor gains energy and there is no instability. The situation changes if we consider a machine operating above transition energy ( $m^* < 0$ ) or the case where the impedance has resistive components (e.g. due to a finite resistivity of the wall). For  $m^* < 0$  we obtain from (240)

$$\Delta\omega_n = \pm i\Delta\omega_I = \pm i \frac{n}{R} \sqrt{\frac{qI_0 X^{sc}}{2\pi |m^*|}}$$

with the imaginary part  $\Delta\omega_I$  of the frequency shift. The unstable situation for  $\Delta\omega_I < 0$  with the instability growth rate

$$\frac{1}{\tau_I} = -\Delta\omega_I$$

is known as the *negative mass instability*<sup>§</sup>. This instability is driven entirely by the the negative mass behavior in circular machines and the space charge

---

<sup>§</sup>Nielsen, Sessler, Symon, Proc. International Conference on High Energy Accelerators, CERN, Geneva, 1959

impedance. Above transition energy a local density increase will grow with time, leading to bunching of the beam.

The momentum spread of the beam causes a diffusion of a local density bump with the decay rate

$$\tau_d^{-1} \approx \frac{n|\eta_0|\beta_0 c(\Delta p/p)}{2\pi R} \quad (241)$$

The instability threshold is then determined through  $\tau_I^{-1} > \tau_d^{-1}$ .

Up to the factor  $2\pi$  and for this criterium for the threshold of the negative mass instability is similar to the *Keil-Schnell stability criterium*<sup>¶</sup>

$$\left| \frac{Z_n}{n} \right| < \frac{mc^2 \beta^2 \gamma |\eta| (\Delta p/p_0)^2}{qI_0} \quad (242)$$

which approximates the instability threshold for real and imaginary impedances  $Z_n = R_n + iX_n$ .

---

<sup>¶</sup>E.Keil, W. Schnell, CERN Report ISR-TH-RF/68-33, CERN, 1968